Engineering Structures 366 (2026) 123347

Contents lists available at ScienceDirect

Engineering Structures

journal homepage: www.elsevier.com/locate/engstruct

A compact isolator for multi-directionally coupled vibration

Mingzhu Jin [a,b], Ge Yan [a], Xiang Yu [a], Xiuhui Hou [c], Zichen Deng [b], Li Cheng [a,*]

[a] Department of Mechanical Engineering, The Hong Kong Polytechnic University, Hong Kong, China
[b] School of Aeronautics, Northwestern Polytechnical University, Xi'an 710072, China
[c] School of Mechanics and Transportation Engineering, Northwestern Polytechnical University, Xi'an 710072, China

ARTICLE INFO

Keywords:
Multi-directional isolator
Coupled vibration
Quasi-zero stiffness
Low-frequency vibration isolation
Nonlinear dynamics

ABSTRACT

Engineering structures are frequently subjected to multi-directional vibrational excitation, calling for the consideration of multi-directional dynamic coupling and its embodiment in vibration isolation design. This paper introduces a 3D-printed integrated isolator designed to attenuate vibrations in two translational and one rotational directions. The structure comprises rigid rods connected by optimized torsional springs to enable three-directional vibration isolation. Corresponding models alongside the solving procedure are developed, followed by dynamic analyses and experimental validations. The proposed isolator is shown to entail effective low-frequency and multi-directional vibration isolation. Vertical direction performance remains robust and amplitude-insensitive, and negligibly affecting the horizontal and rotational directions; whereas horizontal isolation deteriorates under rotational excitation with amplitude-dependent severity and vice versa. The rotational excitation is the primary source of both nonlinearity and static equilibrium position offset. This study offers invaluable insights for designing multi-directional isolators for aerospace and transportation applications.

1. Introduction

Mitigating complex multi-directional vibrations presents a significant challenge in modern engineering applications [1–5]. For example, precision instruments carried by vehicles and aircraft are frequently exposed to dynamic excitations [6] where vibrations occur simultaneously along multiple directions [7–10], due to road surface irregularities, engine forces, and aerodynamic turbulence [11–16]. This compromises the operational stability and passenger comfort, accelerates structural fatigue, and reduces the service life of critical components [17,18]. Consequently, the development of advanced vibration isolation systems allowing for multi-directional vibration attenuation has become a significant research focus [19–21].

Recent advances in vibration isolation have primarily focused on modular systems comprising springs and linkages, including magnetic-driven systems, semi-active electromagnetic isolators, and actively controlled time-delayed isolators [22–31]. Among different options, the strategy based on quasi-zero stiffness (QZS) has been particularly popular. In fact, some designs utilizing flexible straight beams [32], curved beams [33,34], ring thin-walled beams [35,36] and inclined beams [37] were shown to yield the QZS via negative stiffness compensation mechanism, realized through the strategic combination of positive and negative stiffness elements. Other examples include Sui et al. [32], in which a QZS isolator comprising eight flexible beams and a linear spring was proposed. Hou et al. [33] designed a monolithic QZS isolator employing cubic spline flexible beams for multi-load isolation. Xiao et al. [37] developed a 3D-printed QZS isolator with inclined beams to mitigate the typical hardening behavior of QZS isolators. Lu et al. [38] achieved QZS via a dual nonlinear integrating isolator, combining nonlinear negative and positive stiffness structures in parallel. Hussain et al. [39] conceived a QZS damper integrating two anti-symmetrically arranged negative stiffness units with a semicircular positive stiffness arch. Yan et al. [40] achieved QZS by combining linear stiffness elements (linear springs) with nonlinear stiffness components (repulsive magnets) to compensate for the inherent negative stiffness of a rhombus structure, thereby overcoming the limitations of bi-stability. Despite the demonstrated effectiveness, current QZS vibration isolation research primarily focuses on unidirectional vibration control. Consequently, these systems often perform inadequately under complex, multi-directional vibration, demonstrating a clear need for comprehensive multi-directional isolation systems.

Recent research has increasingly focused on multi-directional vibration isolation, predominantly utilizing Stewart platform configurations [41–55]. For example, Sun et al. [41] proposed a QZS

* Corresponding author.
E-mail address: li.cheng@polyu.edu.hk (L. Cheng).

https://doi.org/10.1016/j.engstruct.2026.123347
Received 4 January 2026; Received in revised form 13 May 2026; Accepted 1 July 2026
Available online 6 July 2026

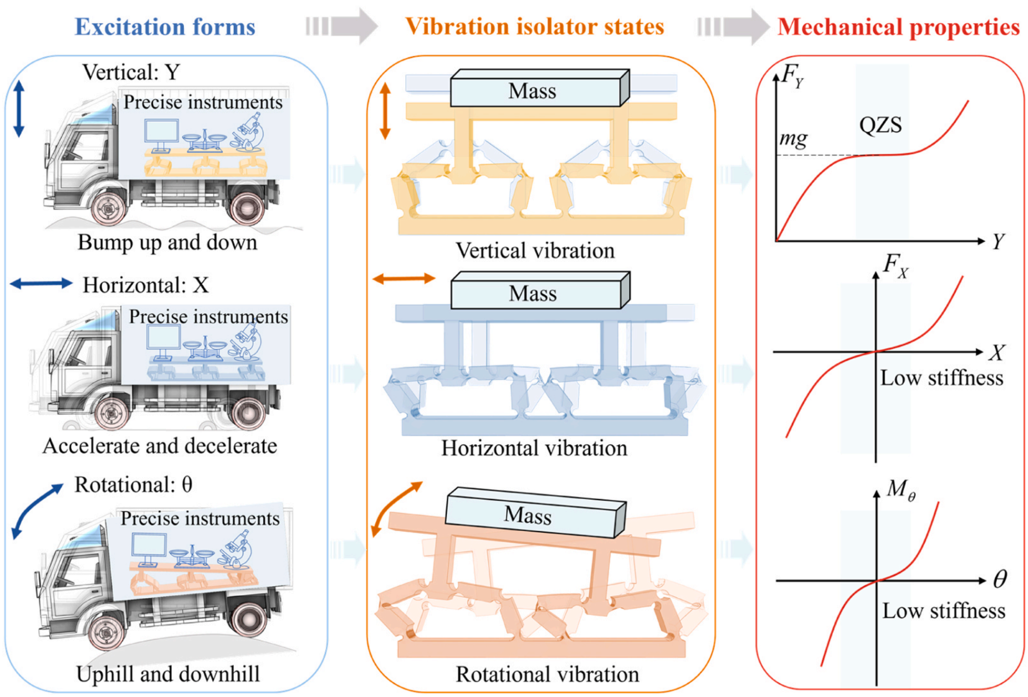

Fig. 1. Background of engineering application and vibration isolation device.

Gough-Stewart isolation platform exhibiting distinct equilibrium positions under different excitation directions. Minh Hung Vu et al. [42] developed a Six Degrees of Freedom (6-DOF) passive vibration isolator based on a Stewart platform with S-shaped legs, providing sufficient load-bearing capacity and isolation performance. Tang et al. [43] designed a 6-DOF parallel strut system with flexible hinges for active vibration control of sensitive optical payloads. Wang et al. [44] presented a general six-bar linkage prototype applicable to axisymmetric four- to six-bar linkage isolation systems. Wu et al. [55] introduced a multi-tile magneto-mechanical spring providing high negative stiffness, effectively reducing resonance frequency to broaden isolation bandwidth.

However, aforementioned systems/platforms encounter inherent limitations: structural bulkiness, excessive weight, complex manufacturing and control requirements, high cost, and environmental sensitivity [56–61]. The friction between components further compromises performance. Crucially, most studies simplify the dynamic models by neglecting the coupling effects or prioritize experimental/numerical results over rigorous theoretical analysis of coupled dynamics. Consequently, a fundamental understanding of the coupled dynamic behavior and its impact on design and isolation performance remain largely insufficient. Among alternative approaches, hinge-link mechanisms have gained attention due to their structural simplicity, flexibility, and potential for achieving tunable, highly coupled stiffness properties [62–64]. While Stewart-platform-based configurations offer 6-DOF isolation capabilities, they often entail complex kinematics and elevated manufacturing costs. Notably, even for some simplified configurations, existing modeling approaches frequently rely on decoupled dynamics or oversimplified assumptions, thereby neglecting a comprehensive treatment of coupled system behavior. Given these challenges, a key research question arises: how can multi-directional vibration isolation be effectively achieved while balancing the model fidelity and modeling effort?

The literature on coupled dynamics in vibration isolation offers a range of valuable theoretical models and perspectives [65–76]. Sun et al. [65] examined the coupled nonlinear dynamics of a QZS Gough-Stewart platform, highlighting that retaining inter-DOF coupling is essential for accurate response prediction. Zhang et al. [66] introduced an asymmetric self-coupled metastructure capable of exciting multiple resonant modes under single-axis input, thus enabling multi-band isolation in a compact form. Xing et al. [67] developed a model predictive control scheme for a 6-DOF rigid-flexible coupled parallel platform, demonstrating active multi-directional isolation. While these works provide important insights into coupling effects, structural design, and active control strategies, the systematic characterization of cross-directional interactions in a fully passive, multi-directional isolator subjected to combined translational and rotational excitations remains an open area.

To address these challenges, this paper presents a compact three-directional vibration isolator and develops a corresponding coupled dynamic model. The proposed three-spring configuration is selected for its distinct advantages in managing vertical, horizontal, and rotational motion. Inspired by biological multi-joint limbs, the three independently adjustable torsional springs achieve vertical QZS while maintaining low stiffness in the lateral and rotational directions. With three independently tunable springs, the design has enough adjustability to regulate stiffness in all three directions without excess complexity, and it remains mechanically concise for ease of fabrication.

With this configuration established, a theory-simulation-experiment framework is employed to uncover the intrinsic multi-directional coupling mechanisms inherent to the system. By examining how these coupling effects influence isolator performance, the work provides fundamental insights into the dynamic behavior of the structure. Key highlights include: (1) Proposing a 3D-printing integrated three-directional isolator which enables low-frequency vibration isolation with efficient, cost-effective fabrication; (2) Revealing the influence of the coupling on vibration isolation performance, and clarifying the interaction mechanisms among different directions; (3) Conducting experimental validation to demonstrate how directional coupling can be leveraged to optimize isolation and mitigate equilibrium offset. This research sheds lights on the underlying physics in multi-directional coupled vibration systems and offers practical guidance for engineering applications.

The present work focuses on a simpler hinge-link mechanism, with an explicit analysis of coupling effects among the X, Y, and θ directions. Compared with two representative Stewart-platform-based multi-

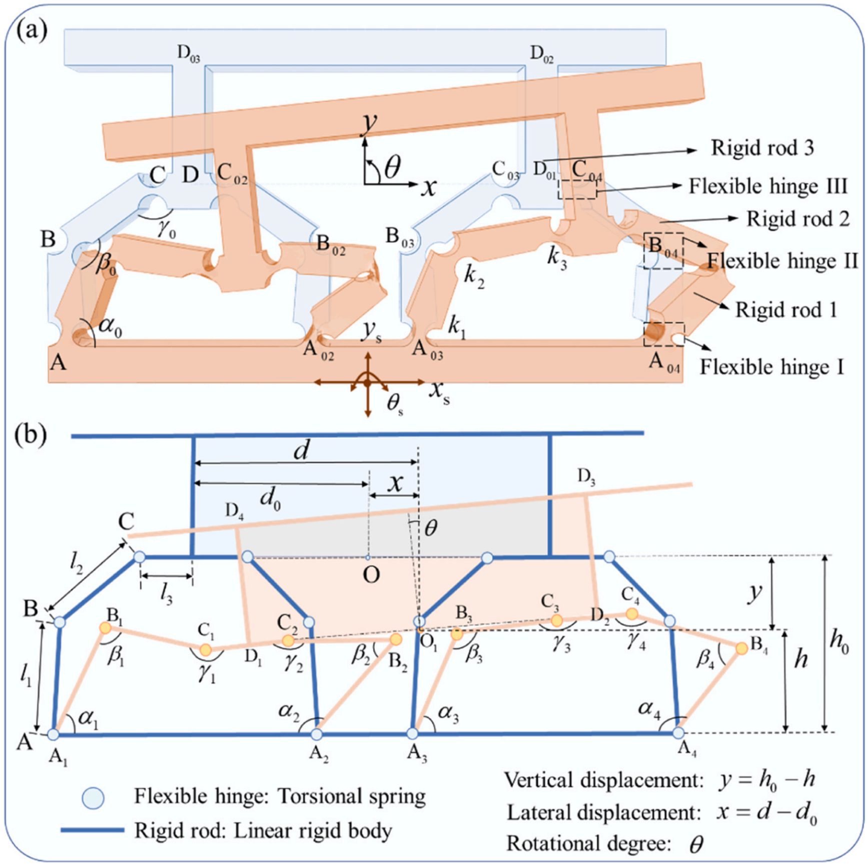

Fig. 2. Kinematic modelling of three-directional vibration isolator: (a) Solid model; (b) Hinged link model.

directional isolators reported in the literature [77,78], the proposed system demonstrates advantages in structural simplicity, reduced manufacturing cost, and fully passive operation, while attaining comparable low-frequency isolation performance. A notable limitation, however, is the reduced number of degrees of freedom (3 versus 6) relative to active Stewart platforms, a trade-off that should be weighed against application-specific requirements.

The remainder of this paper is organized as follows. Section 2 presents the conceptual design of the multi-directional vibration isolator and develops its kinematic and dynamic relationships. Section 3 analyses static stiffness characteristics. Section 4 investigates dynamic responses in vertical (Y), horizontal (X), and rotational (θ) directions and evaluates the vibration isolation performance under various excitation scenarios. Section 5 presents experimental validation of both static stiffness and dynamic response. Finally, Section 6 provides concluding remarks.

2. Conceptual design and modeling

This section summarizes the conceptual design of a multi-directional vibration isolator and lays out the theoretical foundation for its modelling and analysis.

2.1. Design and geometric constraints

Transporting high-precision equipment through complex road environments poses a common engineering challenge. During vehicle operation, equipment is subjected to a variety of excitation forms, thereby generating vertical, horizontal, and rotational motions (Fig. 1). We propose a multi-directional vibration isolator to mitigate these vibrations simultaneously. The design aims to support vertical payloads with high static load capacity while achieving low dynamic stiffness, ideally through QZS behavior. For lateral and pitch vibrations, the objective remains maintaining low dynamic stiffness to minimize vibration transmission.

This isolator, as shown in Fig. 2(a), consists of flexible hinges (I, II, III) and rigid rods (1, 2, 3). Each flexible hinge can provide torsional stiffness. Before modeling the multi-directional vibration isolator, several assumptions are made: 1) The isolation structure is assumed massless, since a mass ratio of 5.99% as compared with the payload mass renders its inertial contribution secondary to that of the payload. 2) All elements are rigid, except the flexible hinges. 3) Analysis is restricted to in-plane deformations (vertical, horizontal, rotational), thereby neglecting out-of-plane behavior.

To facilitate kinematic analysis, isolation system is represented by an equivalent hinged-link model (Fig. 2(b)). Rectangular body $DD_{01}D_{02}D_{03}$ is rigidly connected to the top platform. It undergoes a rigid-body motion from its initial (blue) configuration to its final (orange) configuration, $D_1D_2D_3D_4$, changing only in position and orientation. Flexible hinges are modelled as torsional springs, and rigid rods are treated as rigid bodies. Lengths of three rigid rods are denoted as l_1, l_2, and l_3, respectively. Initial configuration has a height h_0 and central span d_0, becoming h and d, respectively, in the post-deformation. Angular orientations and positional changes during deformation are illustrated in Fig. 2(b).

Geometric relationships are defined as follows:

1) Vertical displacement: Relative vertical position change of the isolation platform, denoted as $y = h_0 - h$;.

2) Horizontal displacement $x = d - d_0$;.

3) Rotational deformation, θ, corresponding to pitch rotation of the platform.

Based on these kinematic relationships, structural motion in three primary directions is analyzed through corresponding kinematic models. The structure is decomposed into four distinct components:

i) Transition from undeformed state (A-B-C-O) to deformed state (A_1-B_1-C_1-O_1), satisfying:

$$\begin{cases} \widehat{x} = \{l_1 \cos\alpha_1 - l_2 \cos(\alpha_1 + \beta_1) + (l_3 + d_0)\cos\theta\} - \{l_1 \cos\alpha_0 - l_2 \cos(\alpha_0 + \beta_0) + l_3 + d_0\} \\ \widehat{y} = \{l_1 \sin\alpha_0 - l_2 \sin(\alpha_0 + \beta_0)\} - \{l_1 \sin\alpha_1 - l_2 \sin(\alpha_1 + \beta_1) + (l_3 + d_0)\sin\theta\} \\ \widehat{\theta} = \theta - \theta_s = \alpha_1 + \beta_1 + \gamma_1 - 2\pi \end{cases}, \tag{1}$$

in which the horizontal, vertical and rotational displacement excitations from the base are x_s, y_s, and θ_s, respectively, as shown in Fig. 2. Relative horizontal, vertical and rotational motions are denoted as $\widehat{x} = x - x_s$, $\widehat{y} = y - y_s$ and $\widehat{\theta} = \theta - \theta_s$, respectively.

ii) Transition from undeformed state A_{02}-B_{02}-C_{02}-O to deformed state A_2-B_2-C_2-O_1, governed by constraint equations:

$$\begin{cases} \widehat{x} = \{-l_1 \cos\alpha_2 + l_2 \cos(\alpha_2 + \beta_2) + (d_0 - l_3)\cos\theta\} + \{l_1 \cos\alpha_0 - l_2 \cos(\alpha_0 + \beta_0) - (d_0 - l_3)\} \\ \widehat{y} = \{l_1 \sin\alpha_0 - l_2 \sin(\alpha_0 + \beta_0)\} - \{l_1 \sin\alpha_2 - l_2 \sin(\alpha_2 + \beta_2) + (d_0 - l_3)\sin\theta\} \\ \widehat{\theta} = \alpha_2 + \beta_2 + \gamma_2 - 2\pi \end{cases}. \tag{2}$$

iii) Transition from undeformed state A_{03}-B_{03}-C_{03}-O to deformed state A_3-B_3-C_3-O_1:

$$\begin{cases} \widehat{x} = \{-l_1 \cos\alpha_0 + l_2 \cos(\alpha_0 + \beta_0) + (d_0 - l_3)\} + \{l_1 \cos\alpha_3 - l_2 \cos(\alpha_3 + \beta_3) - (d_0 - l_3)\cos\theta\} \\ \widehat{y} = \{l_1 \sin\alpha_0 - l_2 \sin(\alpha_0 + \beta_0)\} - \{l_1 \sin\alpha_3 - l_2 \sin(\alpha_3 + \beta_3) - (d_0 - l_3)\sin\theta\} \\ \widehat{\theta} = \alpha_3 + \beta_3 + \gamma_3 - 2\pi \end{cases}. \tag{3}$$

iv) Transition from A_{04}-B_{04}-C_{04}-O to A_4-B_4-C_4-O_1, yielding:

.

$$\begin{cases} \widehat{x} = \{l_1 \cos\alpha_0 - l_2 \cos(\alpha_0 + \beta_0) + (d_0 + l_3)\} - \{l_1 \cos\alpha_4 - l_2 \cos(\alpha_4 + \beta_4) + (d_0 + l_3)\cos\theta\} \\ \widehat{y} = \{l_1 \sin\alpha_0 - l_2 \sin(\alpha_0 + \beta_0)\} - \{l_1 \sin\alpha_4 - l_2 \sin(\alpha_4 + \beta_4) - (d_0 + l_3)\sin\theta\} \\ \widehat{\theta} = \alpha_4 + \beta_4 + \gamma_4 - 2\pi \end{cases}. \tag{4}$$

The above kinematic relationships on system deformation path characterize the geometrical coupling among three directions: vertical, lateral, and rotational motions, which are essential for subsequent coupled dynamic modelling and quantitative evaluation of 3-DOF system's vibration isolation performance.

2.2. Dynamic modeling

Lagrange's approach is adopted for dynamic modelling of the system. Here, we define three generalized coordinates q_i, (where $i = 1, 2, 3$) representing 3-DOF of the isolated platform: $q_1 = \widehat{x} = x - x_s$, $q_2 = \widehat{y} = y - y_s$, $q_3 = \widehat{\theta} = \theta - \theta_s$.

kinetic energy T of the system writes

$$T = \frac{1}{2} m\dot{\widehat{x}}^2 + \frac{1}{2} m\dot{\widehat{y}}^2 + \frac{1}{2} I\dot{\widehat{\theta}}^2. \tag{5}$$

.

Potential energy V comprises the elastic potential energy stored in rotational springs

$$V = \frac{1}{2}\left[\sum_{i=1}^{4} k_1(\alpha_i - \alpha_0)^2 + \sum_{i=1}^{4} k_2(\beta_i - \beta_0)^2 + \sum_{i=1}^{4} k_3(\gamma_i - \gamma_0)^2\right], \tag{6}$$

in which, k_1, k_2 and k_3 are stiffnesses of rotational springs, as shown in Fig. 2(b).

Lagrange's equations, expressed in terms of $L = T - V$, write

$$\frac{d}{dt}\left(\frac{\partial L}{\partial \dot{q}_i}\right) - \frac{\partial L}{\partial q_i} = Q_i \tag{7}$$

in which Q_i is generalized force. Substituting T and V into Eq. (7) yields

$$\begin{cases} \dfrac{\partial L}{\partial \dot{\hat{x}}} = m\dot{\hat{x}},\ \ \dfrac{d}{dt}\left(\dfrac{\partial L}{\partial \dot{\hat{x}}}\right) = m\ddot{\hat{x}},\ \ \dfrac{\partial L}{\partial \dot{\hat{y}}} = m\dot{\hat{y}},\ \ \dfrac{d}{dt}\left(\dfrac{\partial L}{\partial \dot{\hat{y}}}\right) = m\ddot{\hat{y}},\ \ \dfrac{\partial L}{\partial \dot{\hat{\theta}}} = I\dot{\hat{\theta}},\ \ \dfrac{d}{dt}\left(\dfrac{\partial L}{\partial \dot{\hat{\theta}}}\right) = I\ddot{\hat{\theta}} \\ \dfrac{\partial L}{\partial \hat{x}} = -\sum_{i=1}^{4} k_1(\alpha_i - \alpha_0)\dfrac{\partial(\alpha_i - \alpha_0)}{\partial \hat{x}} - \sum_{i=1}^{4} k_2(\beta_i - \beta_0)\dfrac{\partial(\beta_i - \beta_0)}{\partial \hat{x}} - \sum_{i=1}^{4} k_3(\gamma_i - \gamma_0)\dfrac{\partial(\gamma_i - \gamma_0)}{\partial \hat{x}} \\ \dfrac{\partial L}{\partial \hat{y}} = -\sum_{i=1}^{4} k_1(\alpha_i - \alpha_0)\dfrac{\partial(\alpha_i - \alpha_0)}{\partial \hat{y}} - \sum_{i=1}^{4} k_2(\beta_i - \beta_0)\dfrac{\partial(\beta_i - \beta_0)}{\partial \hat{y}} - \sum_{i=1}^{4} k_3(\gamma_i - \gamma_0)\dfrac{\partial(\gamma_i - \gamma_0)}{\partial \hat{y}} \\ \dfrac{\partial L}{\partial \hat{\theta}} = -\sum_{i=1}^{4} k_1(\alpha_i - \alpha_0)\dfrac{\partial(\alpha_i - \alpha_0)}{\partial \hat{\theta}} - \sum_{i=1}^{4} k_2(\beta_i - \beta_0)\dfrac{\partial(\beta_i - \beta_0)}{\partial \hat{\theta}} - \sum_{i=1}^{4} k_3(\gamma_i - \gamma_0)\dfrac{\partial(\gamma_i - \gamma_0)}{\partial \hat{\theta}} \end{cases}, \tag{8}$$

further leading to the following dynamic equations

$$\begin{cases} m\ddot{\hat{x}} + \sum_{i=1}^{4} k_1(\alpha_i - \alpha_0)\dfrac{\partial(\alpha_i - \alpha_0)}{\partial \hat{x}} + \sum_{i=1}^{4} k_2(\beta_i - \beta_0)\dfrac{\partial(\beta_i - \beta_0)}{\partial \hat{x}} + \sum_{i=1}^{4} k_3(\gamma_i - \gamma_0)\dfrac{\partial(\gamma_i - \gamma_0)}{\partial \hat{x}} + c_1\dot{\hat{x}} = -m\ddot{x}_s \\ m\ddot{\hat{y}} + \sum_{i=1}^{4} k_1(\alpha_i - \alpha_0)\dfrac{\partial(\alpha_i - \alpha_0)}{\partial \hat{y}} + \sum_{i=1}^{4} k_2(\beta_i - \beta_0)\dfrac{\partial(\beta_i - \beta_0)}{\partial \hat{y}} + \sum_{i=1}^{4} k_3(\gamma_i - \gamma_0)\dfrac{\partial(\gamma_i - \gamma_0)}{\partial \hat{y}} + c_2\dot{\hat{y}} = -m\ddot{y}_s \\ I\ddot{\hat{\theta}} + \sum_{i=1}^{4} k_1(\alpha_i - \alpha_0)\dfrac{\partial(\alpha_i - \alpha_0)}{\partial \hat{\theta}} + \sum_{i=1}^{4} k_2(\beta_i - \beta_0)\dfrac{\partial(\beta_i - \beta_0)}{\partial \hat{\theta}} + \sum_{i=1}^{4} k_3(\gamma_i - \gamma_0)\dfrac{\partial(\gamma_i - \gamma_0)}{\partial \hat{\theta}} + c_3\dot{\hat{\theta}} = -I\ddot{\theta}_s \end{cases}, \tag{9}$$

where stiffness terms are nonlinear functions of displacements and rotation angles. This necessitates computing complex partial derivatives due to coupled kinematic relationships. Defining the following dimensionless parameters:

$$X = \frac{x}{h_0}, X_s = \frac{x_s}{h_0}, \hat{X} = \frac{\hat{x}}{h_0},\ Y = \frac{y}{h_0}, Y_s = \frac{y_s}{h_0}, \hat{Y} = \frac{\hat{y}}{h_0}, \tag{10}$$

.

Eq. (9) can be rewritten in a dimensionless form as:.

$$\begin{cases} m\ddot{\hat{X}} + k_1\sum_{i=1}^{4}(\alpha_i - \alpha_0)\dfrac{\partial\alpha_i}{\partial \hat{X}} + k_2\sum_{i=1}^{4}(\beta_i - \beta_0)\dfrac{\partial\beta_i}{\partial \hat{X}} + k_3\sum_{i=1}^{4}(\gamma_i - \gamma_0)\dfrac{\partial\gamma_i}{\partial \hat{X}} + c_1\dot{\hat{X}} = -m\ddot{X}_s \\ m\ddot{\hat{Y}} + k_1\sum_{i=1}^{4}(\alpha_i - \alpha_0)\dfrac{\partial\alpha_i}{\partial \hat{Y}} + k_2\sum_{i=1}^{4}(\beta_i - \beta_0)\dfrac{\partial\beta_i}{\partial \hat{Y}} + k_3\sum_{i=1}^{4}(\gamma_i - \gamma_0)\dfrac{\partial\gamma_i}{\partial \hat{Y}} + c_2\dot{\hat{Y}} = -m\ddot{Y}_s \\ I\ddot{\hat{\theta}} + k_1\sum_{i=1}^{4}(\alpha_i - \alpha_0)\dfrac{\partial\alpha_i}{\partial \hat{\theta}} + k_2\sum_{i=1}^{4}(\beta_i - \beta_0)\dfrac{\partial\beta_i}{\partial \hat{\theta}} + k_3\sum_{i=1}^{4}(\gamma_i - \gamma_0)\dfrac{\partial\gamma_i}{\partial \hat{\theta}} + c_3\dot{\hat{\theta}} = -I\ddot{\theta}_s \end{cases}. \tag{11}$$

3. Stiffness analysis

We first perform stiffness analysis on the proposed system in order to elucidate its static properties in delivering QZS functionality. The model will subsequently be integrated into the dynamic model.

3.1. Realization of QZS in Y-direction

For practical isolation structures, two key requirements should be met in Y-direction: high static stiffness for load-bearing and low dynamic stiffness for vibration isolation. As loading capacity in other directions is less required, the design should prioritize Y-direction stiffness, thus requiring analyses of the Y-direction stiffness term in equations of motion to achieve QZS effect.

Kinematic modeling of a unit cell in Y-direction is illustrated in Fig. 3 (solid model in Fig. 3(a) and the corresponding geometric model in Fig. 3(b)). The key geometric parameters governing the system's behavior are the thicknesses of the three flexible hinges, denoted as t_1, t_2, t_3. Each hinge acts as a torsional spring, whose stiffness is determined by the hinge thickness. Hinge linked models before and after deformation are depicted in Fig. 3(c), with geometric dimensions defined in Fig. 3(d). During deformation, the structure undergoes only vertical displacement of rigid bodies about the flexible hinges, with all four components deforming symmetrically and identically. Due to symmetry, the overall static stiffness in Y-direction is obtained by analyzing a single unit cell and multiplying the result by four.

Boundary conditions are: $x = 0$, and $\theta = 0$, and the initial geometry conditions are: $l_1 = 12\text{mm}$, $l_2 = 14\text{mm}$, $l_3 = 5\text{mm}$, $h_0 = 20\text{mm}$, $d_0 = 12\text{mm}$, $\alpha_0 = 0.48\pi$, $\beta_0 = 0.71\pi$, $\gamma_0 = 0.81\pi$. Structure parameters are set as

$$L_1 = \frac{l_1}{h_0} = 0.6,\ L_2 = \frac{l_2}{h_0} = 0.7,\ L_3 = \frac{l_3}{h_0} = 0.15,\ D_0 = \frac{d_0}{h_0} = 0.6. \tag{12}$$

.

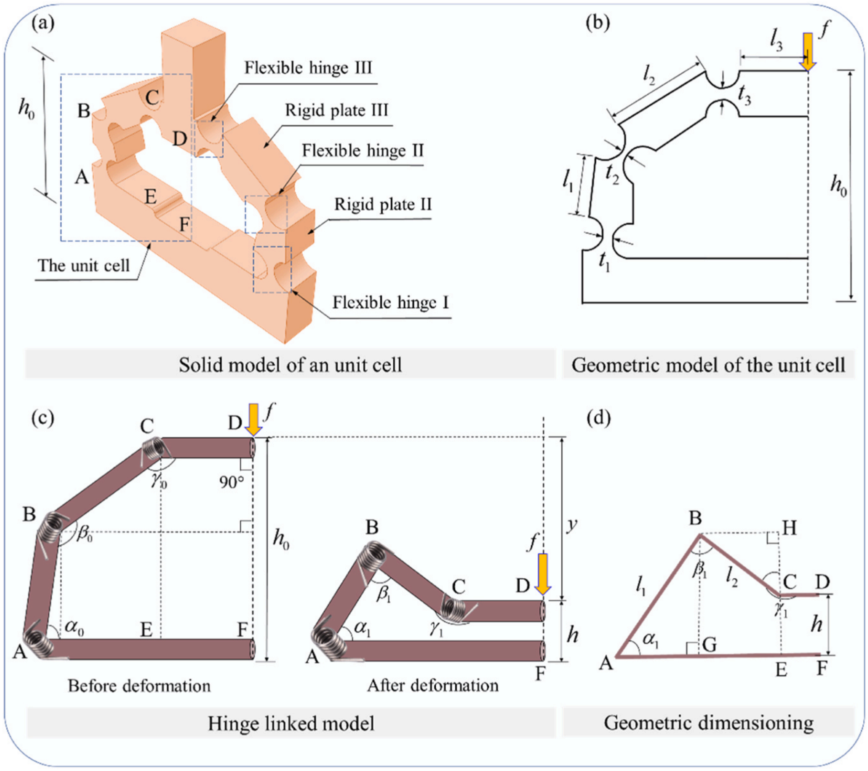

Fig. 3. Kinematic modelling in Y-direction: (a) Solid model of a unit cell; (b) Geometric model of the unit cell; (c) Hinge linked model before and after deformation; (d) Geometric dimension.

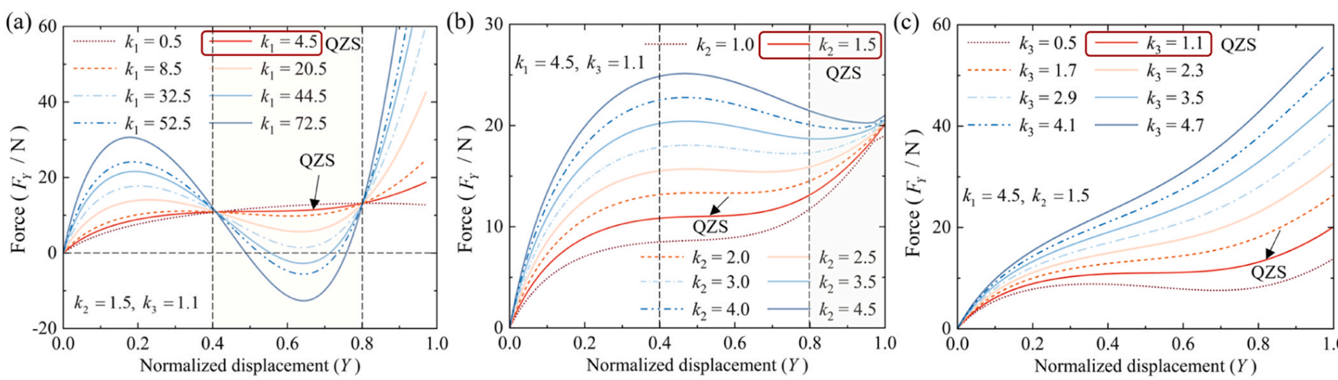

Fig. 4. Effects of key stiffness parameters on the force-normalized displacement curves of the isolator: (a) k_1 of the flexible hinge I; (b) k_2 of the flexible hinge II; (c) k_3 of the flexible hinge III.

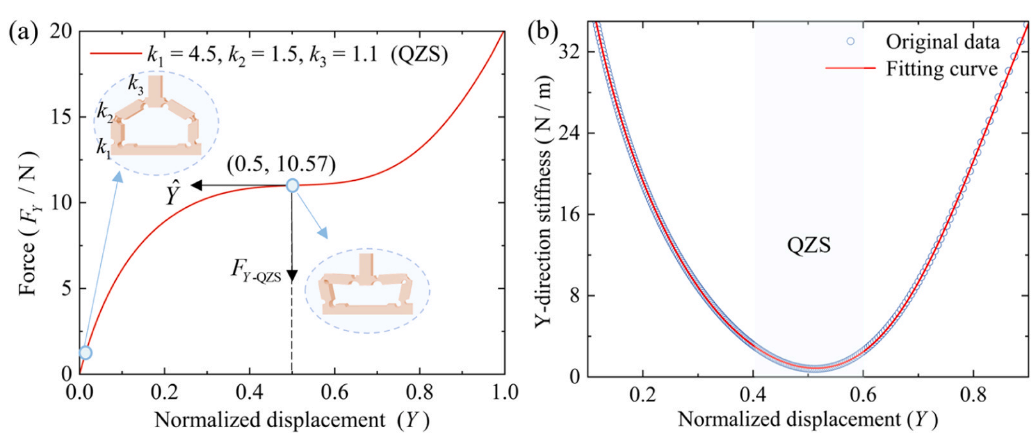

Fig. 5. Realization of QZS in Y-direction: (a) Force-normalized displacement curve; (b) Stiffness curve.

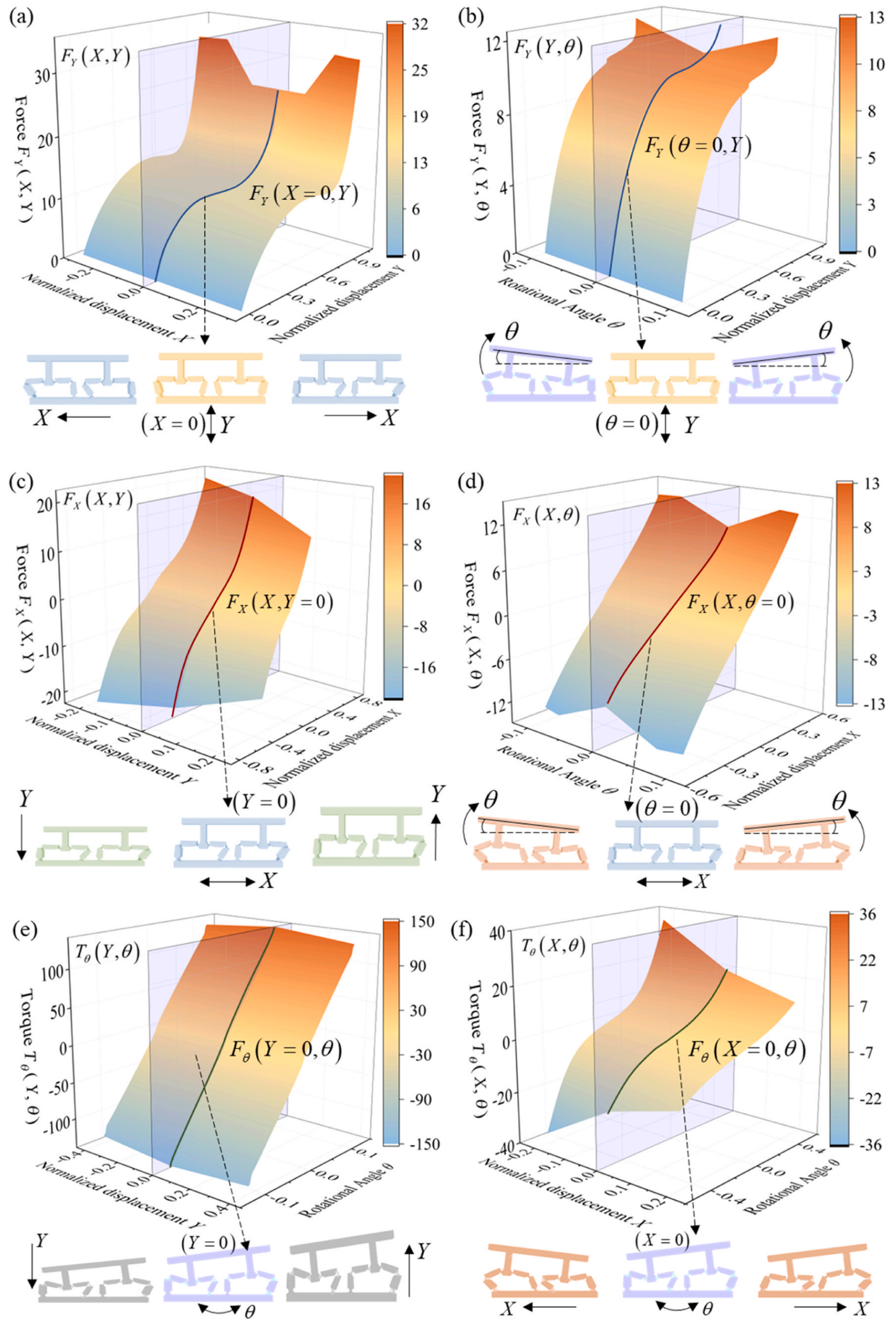

Fig. 6. Stiffness coupling diagrams: (a) $F_Y(X,Y)$; (b) $F_Y(Y,\theta)$; (c) $F_X(X,Y)$; (d) $F_X(X,\theta)$; (e) $F_\theta(Y,\theta)$; (f)$F_\theta(X,\theta)$.

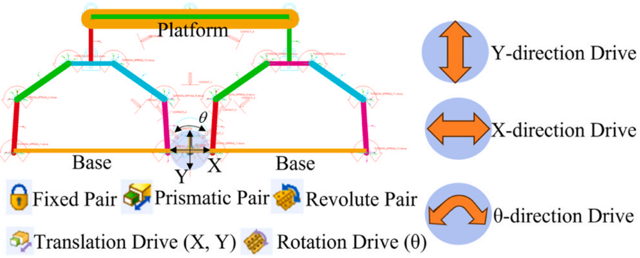

Fig. 7. ADAMS simulation model.

According to the established dynamic relationships (Eq. (11)), the stiffness term along Y-direction writes

$$f = k_1\sum_{i=1}^{4}(\alpha_i-\alpha_0)\frac{\partial\alpha_i}{\partial\widehat{Y}}+k_2\sum_{i=1}^{4}(\beta_i-\beta_0)\frac{\partial\beta_i}{\partial\widehat{Y}}+k_3\sum_{i=1}^{4}(\gamma_i-\gamma_0)\frac{\partial\gamma_i}{\partial\widehat{Y}}. \tag{13}$$

.

Force-normalized displacement curve in Y-direction presented in Fig. 4, which can be segmented into three distinct stages: 0–0.4, 0.4–0.8, and 0.8–1.0. In Fig. 4(a), increasing the stiffness of the flexible hinge I (k_1) amplifies the negative stiffness effect within the intermediate displacement range (0.4–0.8). Conversely, in Fig. 4(b), enhancing the stiffness of flexible hinge II (k_2) further accentuates the negative stiffness effect in the terminal displacement stage (0.8–1.0) when $k_2 = 4.0$ and 4.5. In contrast, an increase in the stiffness of flexible hinge III (k_3) reinforces the positive stiffness response throughout all stages, thereby improving the overall load-bearing capacity of the structure, as depicted in Fig. 4(c).

By tuning the torsional stiffness values of the flexible hinges, the structure exhibits QZS features when the stiffness terms are to $k_1 = 4.5$, $k_2 = 1.5, k_3 = 1.1$, as illustrated in Fig. 5(a). Deformation diagrams of the unit cell at various stages are presented. Force-normalized displacement curve displays a distinct QZS region when the structure is compressed to half its initial height. For more detailed analysis, a local coordinate system (Y-F_{QZS}) is established with its origin at the point (0.5, 10.57 N), which corresponds to the maximum load sustained by the structure in the QZS state and thus defines its load-bearing capacity. Fig. 5(b) further shows the variation of the structural stiffness with compression displacement. Stiffness initially decreases with increasing compression and reaches zero when the deformation attains half of the original height h_0, signifying the realization of the QZS state. Beyond this point, stiffness increases rapidly due to geometric nonlinearities, clearly illustrating the evolving mechanical behavior throughout the deformation process.

Table 1
Quantitative error metrics between RK4 and ADAMS results.

Direction	Δf_p (Hz)	δf_p (%)	e_A (%)	RMSE	NRMSE (%)
Y	0.10	4.08%	4.35%	0.008	1.21%
X	0.16	4.36%	4.79%	0.012	1.82%
θ	0.13	4.25%	3.30%	0.006	1.14%

3.2. Stiffness coupling characteristics

In light of the required high static load-bearing capacity and low dynamic characteristics in Y-direction, the stiffness coupling terms in the dynamic equations are further analyzed. To intuitively demonstrate the influence of coupling effects on the structural static stiffness, several three-dimensional force-normalized displacement curves are plotted. For instance, $F_Y(X, Y)$denotes the Y direction force generated by the normalized displacements in both X and Y directions. Similarly, $F_Y(Y,\theta)$, $F_Y(X,Y,\theta)$; $F_X(X,Y)$, $F_X(X,\theta)$, $F_X(X,Y,\theta)$;$F_\theta(X,\theta)$, $F_\theta(Y,\theta)$ and $F_\theta(X,Y,\theta)$ can also be obtained to analyze other coupling effects. By visualizing the influence of multi-directional displacements on the force developed in a specific direction, the structural coupling behavior is elucidated.

Fig. 6(a) shows the variation of$F_Y(X,Y)$. The curve passing through the central rectangular box represents the force-normalized displacement response in the Y direction when the normalized displacement in X direction is zero, which is consistent with the results presented in Fig. 5(a). Crucially, the Y-direction force-displacement curve remains effectively unchanged under left or right translational displacement along the X-direction. This indicates minimal impact of the X-direction displacement on Y-direction stiffness, demonstrating negligible cross-axis coupling effect from X-direction vibrations on the Y-direction dynamic response. This conclusion will be further validated in vibration isolation performance analysis (Section 4).

Effect of rotational coupling (θ) on the force in the Y direction is illustrated in Fig. 6(b). Rotational displacement induces a slight increase in the Y-direction stiffness due to deviation from the static equilibrium position. Surface plot (most pronounced in Fig. 6(d)) reveals a concave center flanked by convex regions when the force is positive, suggesting significant effects of the rotational coupling on X-direction stiffness. Simultaneous translation and rotation further displace the structure from equilibrium, while increasing stiffness. A similar translational-rotational coupling effect is observed for the X-direction translation on the rotational stiffness in Fig. 6(f). In contrast, Y-direction coupling negligibly influences the stiffnesses in X or θ directions, as confirmed by Fig. 6(c) and Fig. 6(e).

Multi-directional coupling significantly influences the directional stiffness properties, which substantially affect the structure's dynamic response. Specifically, rotational coupling (θ) exerts a pronounced effect on the stiffness in other directions, evidenced by the slope variations in Fig. 6(b) and Fig. (d). In contrast, the translational coupling in Y-

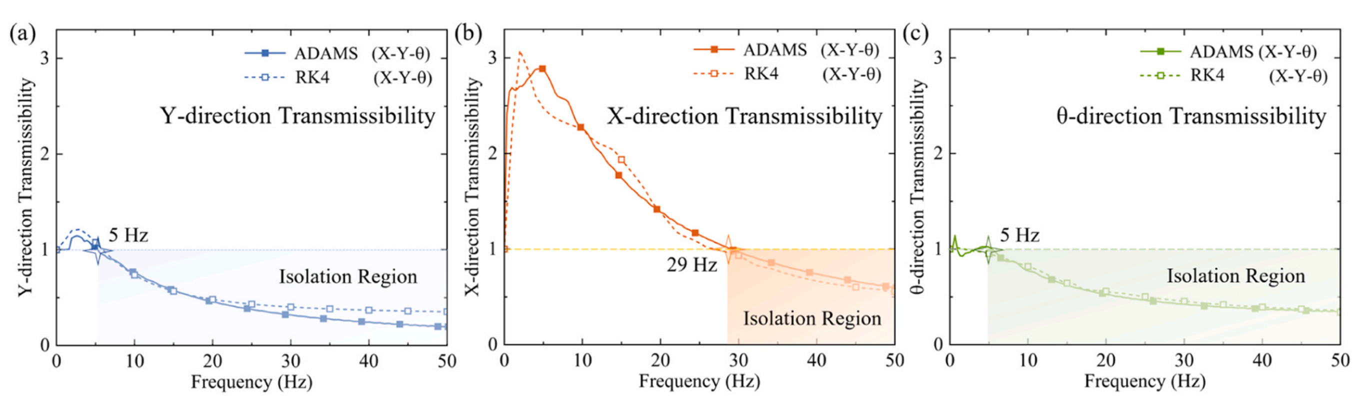

Fig. 8. Comparisons between ADAMS and RK4 results: (a) Y-direction transmissibility; (b) X-direction transmissibility; (c) θ-direction transmissibility.

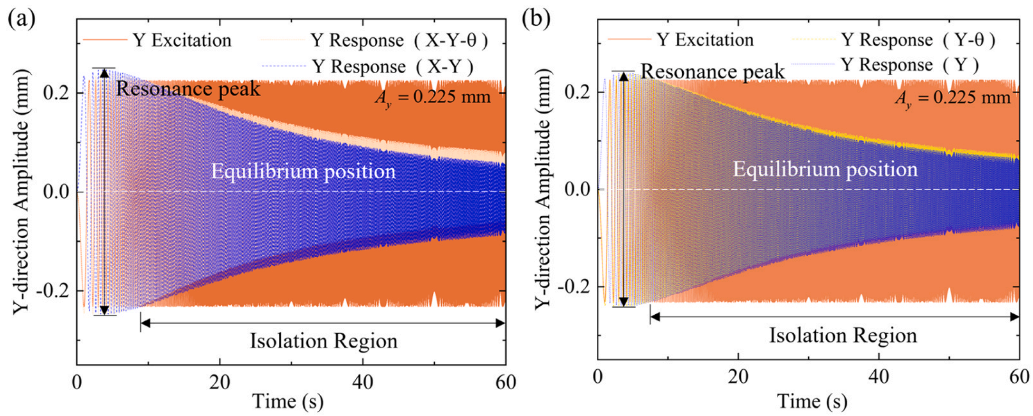

Fig. 9. Time-domain responses in Y direction under different base excitations: (a) Y-direction time-domain responses under X-Y-θ three-directional excitations, and under X-Y two-directional excitations; (b) under Y-θ two-directional excitations, and under Y single-directional excitation.

direction exhibits negligible cross-coupling effects on other directions, as shown in Fig. 6(c) and Fig. (e). X-direction translation minimally influences Y-direction stiffness (Fig. 6(a)) but significantly affects the rotational stiffness (Fig. 6(f)). These findings highlight that a thorough understanding of the coupling mechanisms is essential to achieve accurate dynamic prediction, enabling optimized structural design for enhanced isolation performance under multi-directional excitations.

4. Dynamic analyses

Analyses are carried out to first validate the established model, and the elucidate the salient dynamic features of the proposed isolator, in views of multi-directional vibration isolation.

4.1. Verification and comparison

This section validates the numerical solution of RK4 using an ADAMS simulation model (Fig. 7). The model includes five fixed pairs on the upper platform, two prismatic pairs on the base platform, and twelve revolute pairs at rotational hinges. Translational drives in the X and Y directions and a rotational drive in θ are applied to simulate the coupling dynamic excitation.

Fast Fourier transform (FFT) is applied to the displacement time-history data of both excitation and response to obtain frequency-domain spectra. Transmissibility [62,63] is calculated as the ratio of platform displacement to the base displacement. As shown in Fig. 8, the transmissibility curves derived from both methods under simultaneous three-directional excitations show close agreement. Isolation

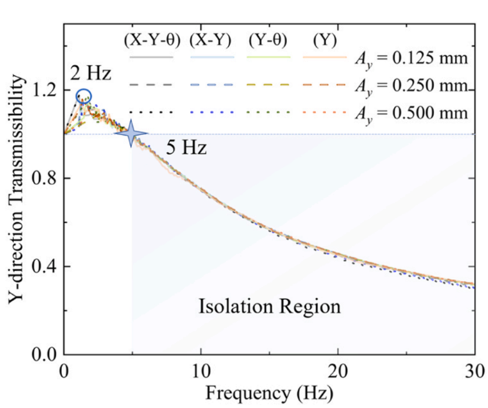

Fig. 10. Frequency-domain responses in Y direction under different base excitations and different excitation amplitudes.

performance is optimal in the Y-direction, but poorer in the X-direction, likely due to stronger coupling effects from θ-direction excitation on the X-direction, a point to be further discussed in subsequent sections. Both Y- and θ-directions exhibit lower resonance peaks and the starting isolation frequency of 5 Hz, whereas the X-direction shows higher resonance and a higher starting isolation frequency.

Having validated the accuracy of the model upon applying three-directional excitations simultaneously, the isolation performance in each direction is further analyzed under various excitation conditions.

To quantitatively validate the RK4 numerical model against ADAMS simulations, the following error metrics are employed. For each dominant resonance peak in the transmissibility curves, the peak frequency difference (Δf_p) between RK4 and ADAMS results is computed as

$$\Delta f_p = \left| f_p^{RK4} - f_p^{ADAMS} \right|, \tag{14}$$

which is expressed as a percentage relative to the ADAMS peak frequency:

$$\delta f_p(\%) = \frac{\Delta f_p}{f_p^{ADAMS}} \times 100\%. \tag{15}$$

.

The relative error in transmissibility magnitude at each resonance peak is calculated as

$$e_A(\%) = \frac{\left| T^{RK4}\left(f_p\right) - T^{ADAMS}\left(f_p\right) \right|}{T^{ADAMS}\left(f_p\right)} \times 100\%. \tag{16}$$

.

Root-mean-square error (RMSE) over the entire frequency range of interest:

$$\mathrm{RMSE} = \sqrt{\frac{1}{N}\sum_{i=1}^{N}\left[T^{RK4}(f_i) - T^{ADAMS}(f_i)\right]^2}, \tag{17}$$

where N is the number of frequency sampling points. The normalized RMSE (NRMSE) is also defined as

$$\mathrm{NRMSE} = \frac{\mathrm{RMSE}}{\max\left(T^{ADAMS}\right) - \min\left(T^{ADAMS}\right)} \times 100\%. \tag{18}$$

.

As shown by different metrics in Table 1, the RK4 numerical solution agrees well with the ADAMS simulation, with peak frequency deviations and amplitude errors generally within 5%. The small discrepancies are attributed to the different solvers (adaptive step-size in ADAMS vs. fixed-step RK4) and minor differences in the implementation of the damping model, which do not affect the main physical conclusions.

4.2. Isolation performance in Y direction

A comparative analysis of Y-direction dynamic response is conducted under both single and multi-directional excitations. Base excitations are applied in Y-direction with amplitudes of 0.125 mm, 0.225 mm, and 0.500 mm, respectively, using a 0–30 Hz sine sweep over 60 s.

In the simulation, all torsional springs were assigned a damping constant of 0.12N·mm·s/rad. This small value approximates frictional energy dissipation in rotational joints and introduces minor artificial damping to improve numerical stability without altering the dominant dynamics. In multi-direction excitation cases, amplitudes in the other two directions are set to 0.35 mm (X) and 0.01 rad (θ). Fig. 9 shows Y-direction time-domain responses under different excitation conditions (illustrated for $A_y = 0.225$ mm, excitation in other directions exists but is not shown in the figure, as the vibration isolation performance in Y direction is the focus of discussion here first), where "X-Y-θ" denotes simultaneous excitation in all three directions. The results demonstrate a low resonance peak and rapid achievement of effective vibration isolation in Y-direction.

As shown in Fig. 10, frequency-domain responses in Y-direction under different base excitations and excitation amplitudes consistently indicate a resonance frequency of approximately 2 Hz and the starting isolation frequency around 5 Hz. This demonstrates notable robustness in the Y-direction, which serves as the principal axis for both static load support and dynamic isolation. The stability of the isolation performance under varied excitation conditions stems from the structural design and parametric configuration of the isolator, which effectively decouples the Y-direction from other degrees of freedom, minimizing vibrational energy transfer from the coupled directions. This characteristic ensures consistent Y-direction isolation performance, making the isolator particularly suitable for applications requiring high load-bearing and vibration isolation along a primary axis.

Fig. 11 shows the velocity-displacement phase diagrams in Y-direction under different excitation conditions. Elliptical trajectories confirm the quasi-harmonic oscillation about the equilibrium point. Vibration starts at the origin, reaches maximum amplitude at resonance, and gradually decays toward equilibrium. A significant equilibrium shift occurs under X-Y-θ excitation (Fig. 11(a)), while negligible deviation is observed under X-Y or Y-θ excitation (Fig. 11(b)). X-Y-θ excitation also reduces Y-direction velocity due to energy redistribution among coupled modes. The close similarity between Y-θ and single Y-direction responses indicates the weak influence from rotational excitation. These phenomena result from dynamic coupling among translational and rotational degrees of freedom, which introduces additional stiffness coupling terms, altering the force distribution and system equilibrium.

To quantitatively assess directional coupling effects, the influence of X- and θ-direction amplitudes on Y-direction transmissibility under various excitation conditions is analyzed. Fig. 12 (a) shows the effect of X-direction amplitude under X-Y-θ and X-Y conditions. Fig. 12(b) illustrate the effect of θ-direction amplitude under X-Y-θ and Y-θ conditions,

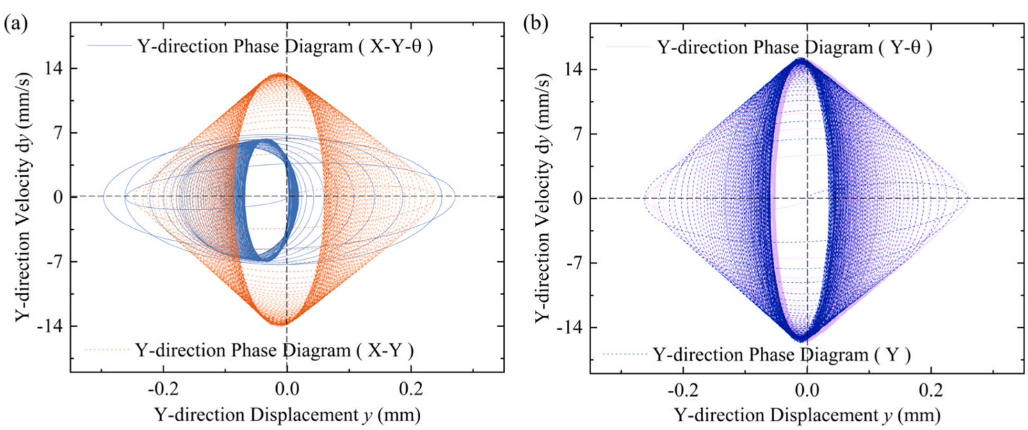

Fig. 11. Velocity-displacement phase diagram of Y direction response under different base excitations: (a) X-Y-θ excitations and X-Y excitations; (b) Y-θ excitations and Y single-directional excitation.

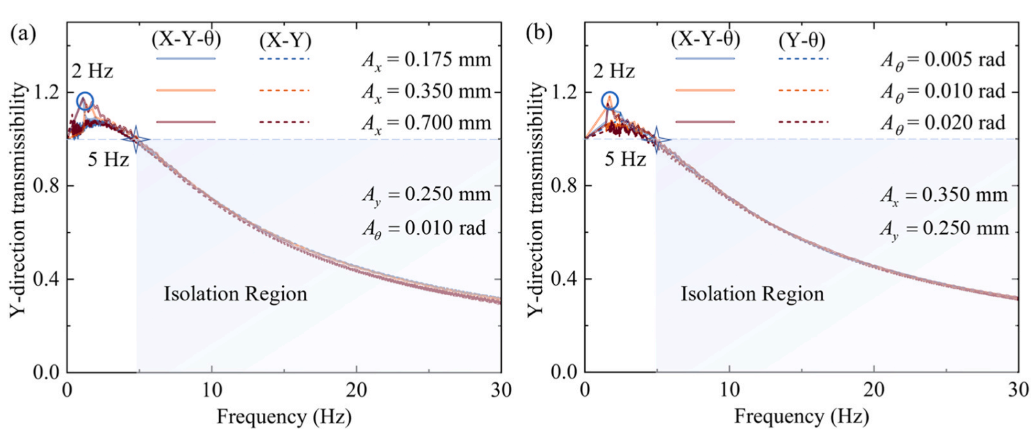

Fig. 12. Influence of X- and θ-direction amplitudes on Y-direction transmissibility under different excitation conditions: (a) effect of X-amplitude under X-Y-θ and X-Y conditions; (b) effect of θ-amplitude under X-Y-θ and Y-θ condition.

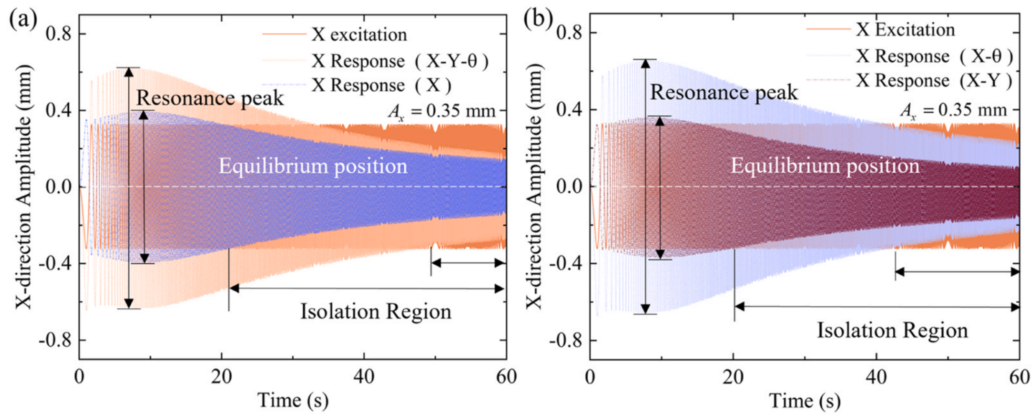

Fig. 13. Time-domain responses in X direction under different base excitations: (a) comparison between X-Y-θ excitations and single X-directional excitation; (b) comparison between X-θ excitations and X-Y excitations.

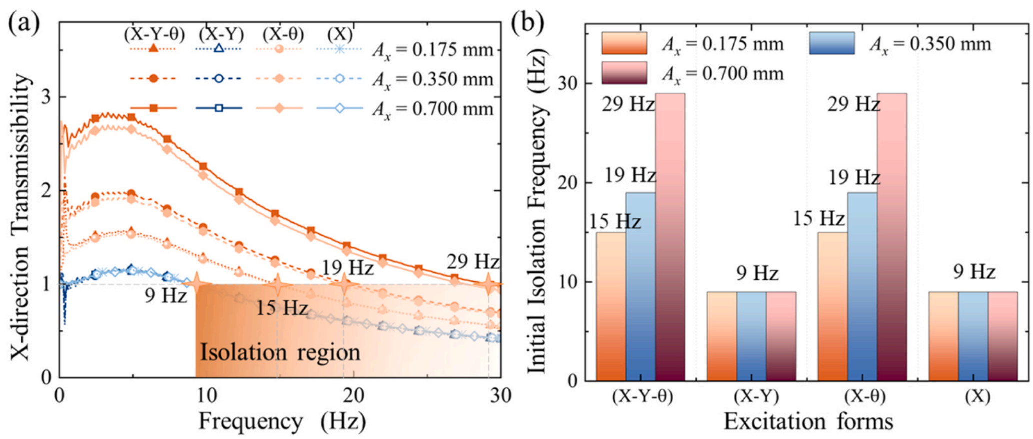

Fig. 14. Frequency-domain response of the X direction under different types of excitations and three levels of excitation amplitudes: (a) Transmissibility curves; (b) starting isolation frequency.

while holding the other excitation amplitudes constant. The transmissibility curves demonstrate that amplitude variations in the X- and θ-directions have negligible effects on Y-direction isolation performance, confirming the robustness of the isolator in the Y-direction under multi-directional excitation.

4.3. Isolation performance in X direction

Vibration isolation performance in X-direction is further analyzed under various excitations. Applied X-direction excitation amplitudes are 0.175 mm, 0.35 mm, and 0.70 mm, with a 0–30 Hz sine sweep over 60 s. For multi-directional excitations, amplitudes in the other directions are maintained at 0.25 mm (Y) and 0.01 rad (θ). Fig. 13 shows the X-direction time-domain responses under different excitations. The

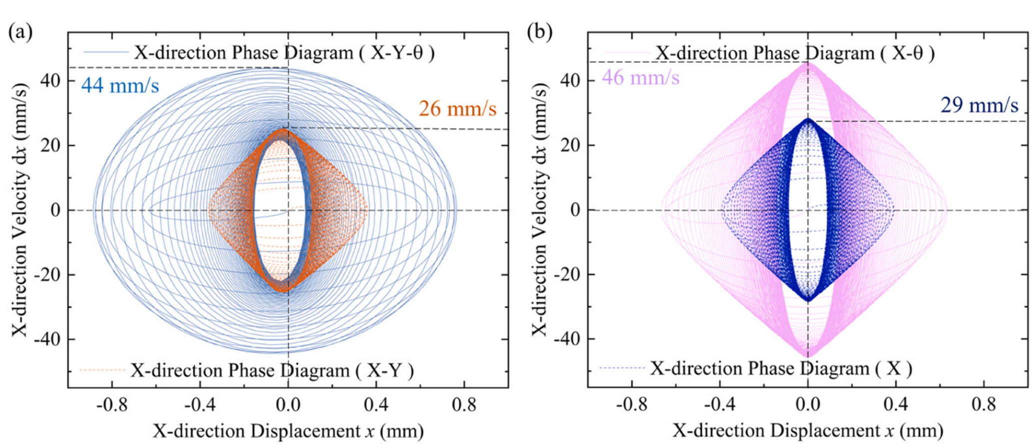

Fig. 15. Velocity-displacement phase diagrams in X direction under different base excitations: (a) X-Y-θ and X-Y excitations; (b) X-θ excitations and X single-directional excitation.

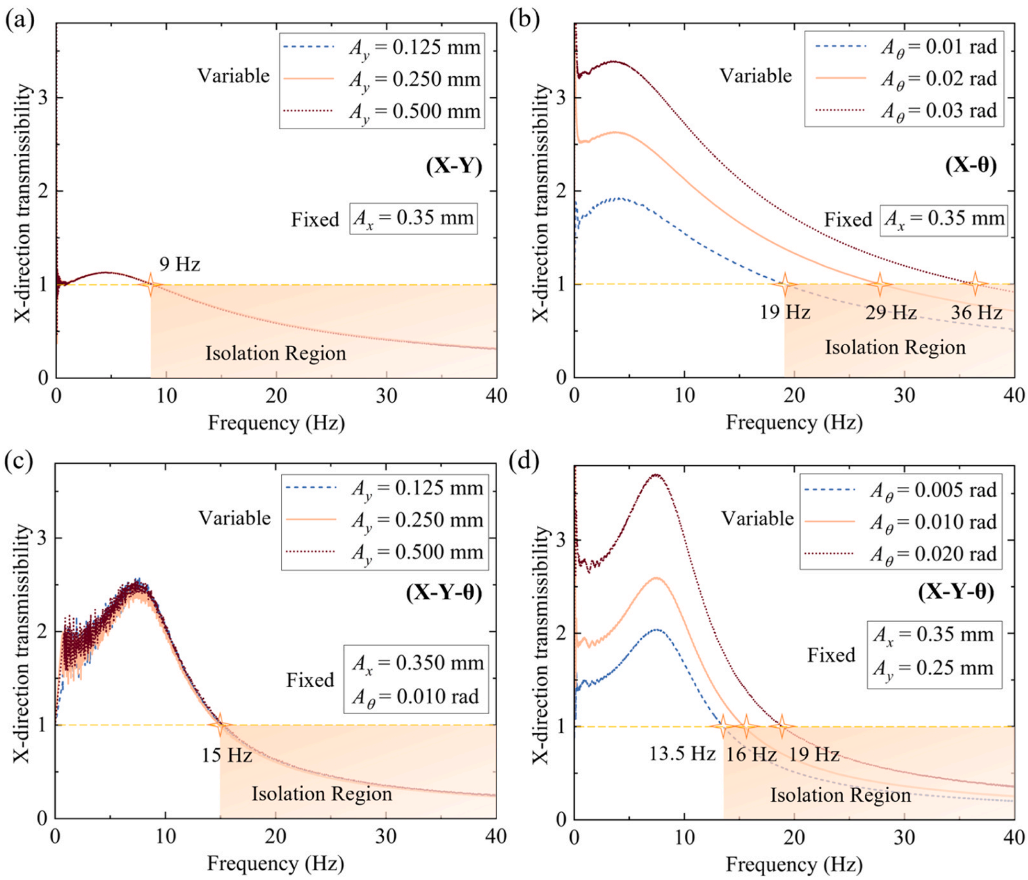

Fig. 16. Influence of Y- and θ-direction amplitudes on X-direction transmissibility under different excitation conditions: (a) effect of Y-amplitude under X-Y condition; (b) effect of θ-amplitude under X-θ condition; (c) effect of Y-amplitude under X-Y-θ condition; (d) effect of θ-amplitude under X-Y-θ condition.

response under X-Y-θ excitation exhibits higher resonance peaks and stronger oscillations compared to single X-direction excitation. Similarly, X-θ condition produces a more intense response than X-Y condition. Notably, responses under X-Y-θ and X-θ excitations are highly similar, indicating that θ-direction coupling dominates X-direction dynamics, while Y-direction coupling has negligible influence. This is further supported by the close match between single X and X-Y excitation responses. The amplified response under θ-involved excitations is attributed to inertial and stiffness coupling between rotational and translational degrees of freedom. Energy transferred from θ-directional excitation intensifies X-direction resonance, whereas Y-directional leads to minimal coupling effect on X-directional response.

Fig. 14(a) compares X-direction transmissibility under different excitation types and amplitudes. Under X-Y-θ and X-θ excitations, the starting isolation frequency in the X-direction increases with increasing excitation amplitude (from approximately 15 Hz to 29 Hz). In contrast, transmissibility remains stable under X-Y or X excitation conditions, indicating linear behavior in X-direction. These results confirm that θ-directional coupling significantly influences X-directional dynamics, while Y-directional excitation has negligible effect.

Fig. 15 shows velocity-displacement phase diagrams in X-direction under different excitations. Three-directional (X-Y-θ) excitation increases velocity amplitude, amplifies resonance, and degrades isolation performance in X-direction. In contrast, the response under X-Y condition closely resembles that under single X excitation, confirming the negligible effect of Y-direction coupling. Under X-θ excitation, the velocity near equilibrium remains high (approx. 46 mm/s), indicating strong rotational coupling. Replacing θ with Y excitation (i.e., X-Y condition) reduces the velocity near equilibrium to about 26 mm/s, half that under X-θ condition. In summary, θ-direction coupling exacerbates X-direction vibration, while coupling in the Y-direction exerts a negligible influence on isolation performance.

Fig. 16 examines the influence of Y- and θ-direction amplitudes on X-direction transmissibility under different excitation conditions. As shown in Fig. 16(a), variations in Y-direction amplitude have negligible effect on X-direction transmissibility. In contrast, Fig. 16(b) suggests that increasing θ-direction amplitude elevates X-direction transmissibility, indicating degraded isolation performance with stronger rotational coupling. Under X-Y-θ condition with fixed X and θ amplitudes (Fig. 16(c)), changes in Y-direction amplitude again show minimal impact. However, when θ-direction amplitude increases under three-direction excitation condition (Fig. 16(d)), X-direction isolation deteriorates and the starting isolation frequency shifts upward, confirming the dominance of θ-coupling in X-direction dynamics.

4.4. Isolation performance in rotation (θ direction)

With excitation amplitudes in X and Y directions being fixed at 0.175 mm and 0.25 mm, respectively, θ-direction amplitude is varied (0.01 rad, 0.02 rad, 0.10 rad). Dynamic response in θ-direction is analyzed, with time-domain results shown in Fig. 17. Under three-directional excitations, a persistent equilibrium shift of approximately 0.007 rad occurs in θ-direction. This deviation arises primarily from the relatively large translational excitations in X and Y directions, which induce inertial forces and moments that disturb the rotational equilibrium.

Fig. 18 shows that multi-directional excitation slightly elevates the θ-direction resonance peak and starting isolation frequency. The X-direction excitation notably influences the θ-response, whereas the Y-direction has negligible effect, indicating that X-θ coupling dominates over

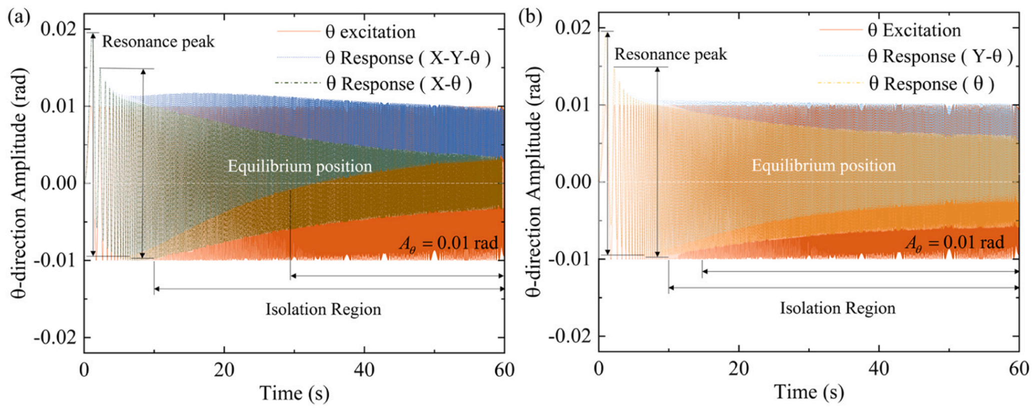

Fig. 17. Time-domain responses in θ direction under different base excitations: (a) X-Y-θ and X-θ excitations; (b) Y-θ and single θ-directional excitations.

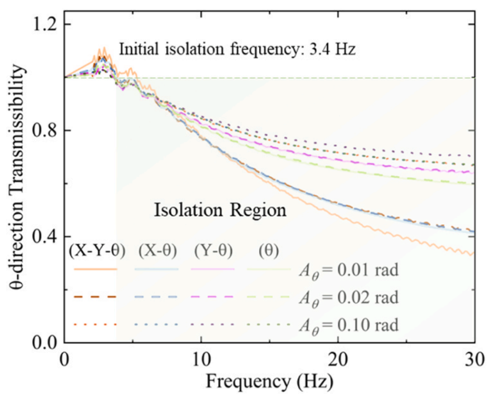

Fig. 18. Frequency-domain responses in the θ direction under different base excitations and different excitation amplitudes.

Y-θ coupling.

Fig. 19 presents velocity-displacement phase diagrams in the θ-direction under different excitation conditions. Asymmetric trajectories are observed in all cases, indicating a deviation from the initial static equilibrium during vibration, leading to inconsistent bilateral displacements and the formation of asymmetric cusps. Under X-Y-θ condition, the phase diagram exhibits significant complexity, eventually converging to an inclined ellipse, reflecting strong nonlinear interactions and a substantial shift from equilibrium. Comparative analysis reveals that X-θ condition reduces the angular velocity near equilibrium to half of that under single θ excitation (Fig. 19 (b)), while Y-θ condition shows similarity with the phase diagram of θ-direction. This suggests that X-direction coupling effectively dissipates vibrational energy through damping or stiffness constraints, thereby attenuating rotational motion, whereas Y-direction coupling has minimal energy transfer effect. Findings emphasize the necessity of incorporating coupling effects and nonlinear behavior in the analysis and design of vibration isolation systems.

Fig. 20 examines influence of X- and Y-direction amplitudes on θ-direction transmissibility under different excitation conditions. As shown in Fig. 20 (a), increasing X-direction amplitude from 0.175 mm to 0.700 mm under X-θ condition raises θ-direction transmissibility and shifts the starting isolation frequency from 4.5 Hz to 9 Hz, indicating degraded isolation performance with stronger X-direction coupling. In contrast, Fig. 20 (b) shows that under Y-θ condition, higher Y-direction amplitudes reduce transmissibility beyond 4.5 Hz, with optimal isolation observed at 0.500 mm, suggesting a beneficial coupling effect from Y-direction. Under three-directional X-Y-θ condition (Fig. 20 (c)), larger X-amplitudes worsen θ-direction isolation, increasing both resonant peak and starting isolation frequency (up to 26 Hz). Conversely, Fig. 20 (d) shows that increasing Y-amplitude improves θ-direction isolation, lowering the starting isolation frequency (from 13 Hz to 11.5 Hz) and reducing transmissibility. These results confirm that X-direction coupling impairs θ-direction isolation, while Y-direction coupling enhances it, consistent with findings in Figs. 17 and 18.

5. Experiments

A proof-of-concept prototype was fabricated using silicone molding with thermoplastic polyurethane (TPU) material. This approach offers

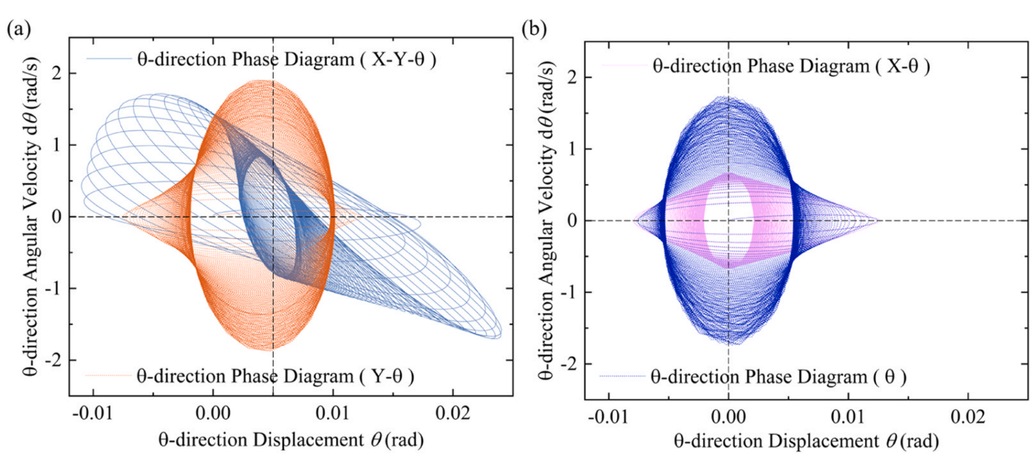

Fig. 19. Velocity-displacement phase diagram of θ direction under different base excitations: (a) X-Y-θ and Y-θ excitation; (b) X-θ and θ single-directional excitations.

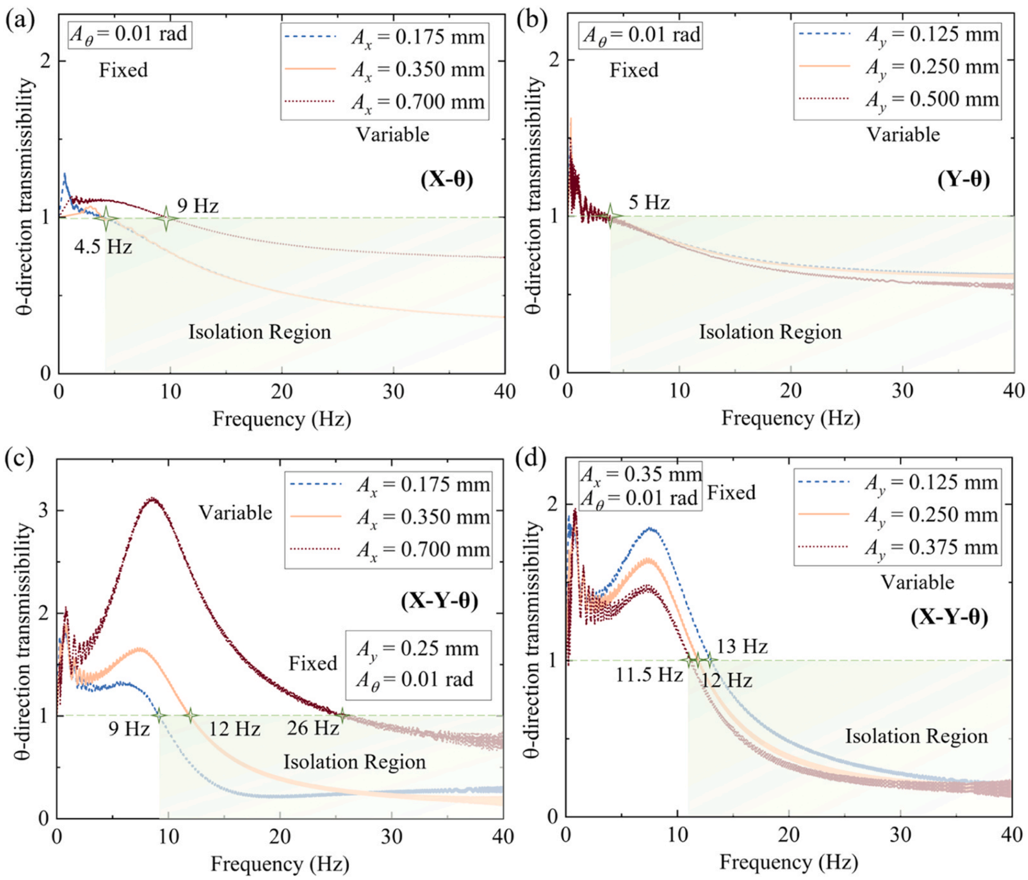

Fig. 20. Influence of X- and Y-direction amplitudes on θ-direction transmissibility under different excitation conditions: (a) effect of X-amplitude under X-θ condition; (b) effect of Y-amplitude under Y-θ condition; (c) effect of X-amplitude under X-Y-θ condition; (d) effect of Y-amplitude under X-Y-θ condition.

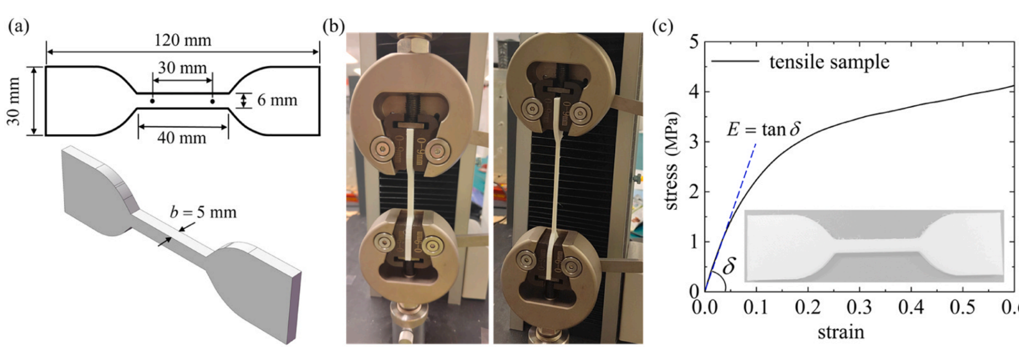

Fig. 21. Tensile experiment of TPU: (a) Tensile sample, (b) Tensile experimental, (c) Stress-strain curve.

rapid production, high replication fidelity for complex geometries, cost-effectiveness for small batches, and utilizes a material capable of large deformations and high flexibility. As shown in Fig. 21 (a)-(b), specimen geometry and testing parameters were designed in accordance with relevant standards to ensure reliable and reproducible tensile performance evaluation. Stress-strain curve, presented in Fig. 21 (c), is used to characterize mechanical behavior of TPU. Young's modulus, derived from the slope of the linear elastic region, is determined to be 20 MPa. A summary of the material properties obtained from these tests is provided in Table 2. All properties are measured following applicable ASTM or ISO standards to ensure accuracy and validity.

Table2
TPU material properties.

Material	E (MPa)	ρ (kg/m^3)	ν
TPU	20.00	1.18	0.40

5.1. Static experiments

Static stiffness of 3D-printed specimens was first evaluated along X, Y, and θ directions using a universal testing machine under quasi-static displacement-controlled loading at 2 mm/min (Fig. 22). Under Y-direction loading, the structure exhibits QZS within the dimensionless displacement range of 0.4–0.6. As shown in Fig. 22(b), force-normalized displacement curves from theoretical, numerical, and experimental analyses demonstrate strong agreement. To characterize stiffnesses in X and θ directions, the structure is maintained at the QZS state in Y-direction by applying a constant weight of 1.086 kg. For X-direction, a pulley-rope system converts a vertical tensile force into a horizontal

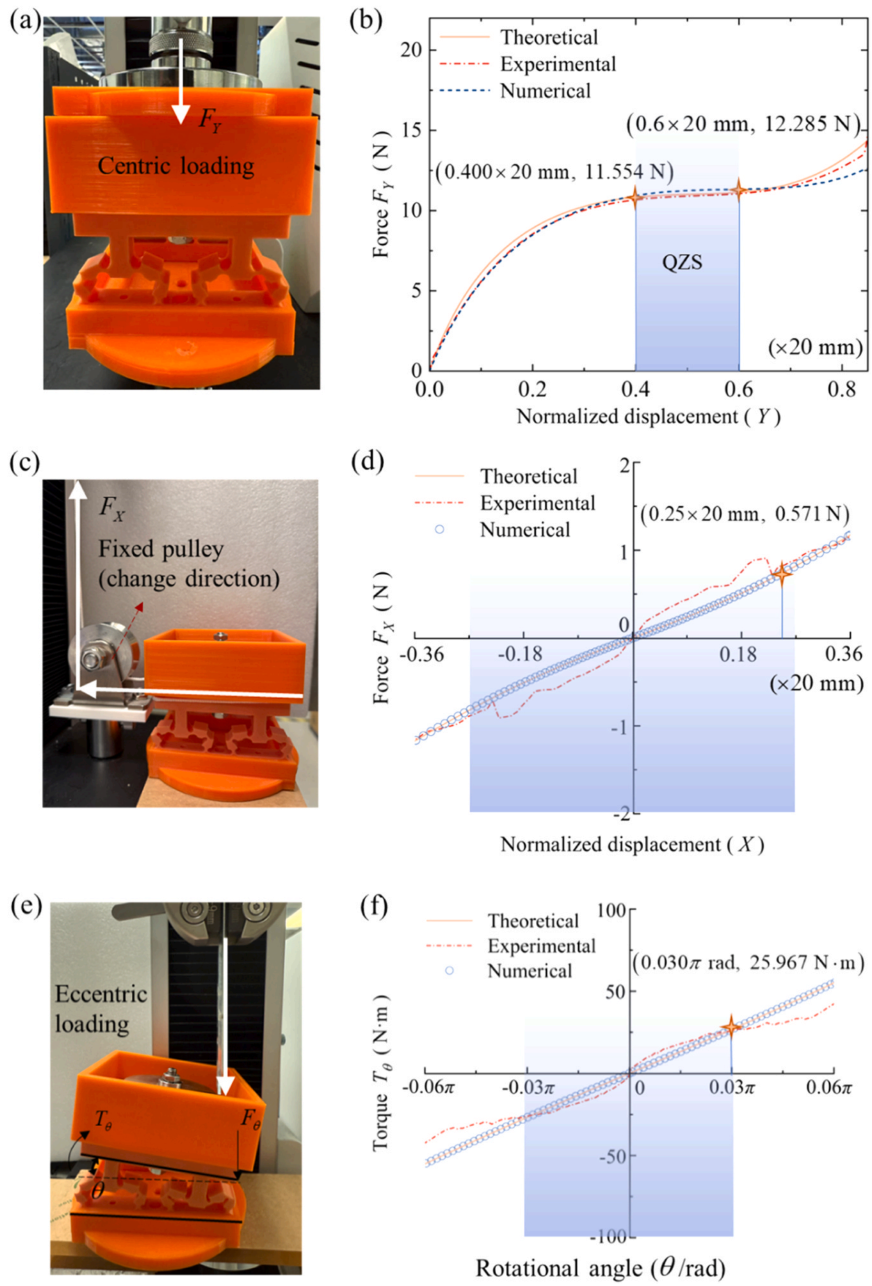

Fig. 22. Static experiments and force-displacement curves in three directions: (a)-(b) Y-direction; (c)-(d) X-direction; (e)-(f) θ-direction.

loading. Force-normalized displacement curves (Fig. 22(c)-(d)) show generally good agreement across methods, with minor deviations due to experimental tilting. Torsional stiffness (θ direction) is measured via applying an eccentric loading, with force and displacement converted to torque and rotation angle. Torque-rotation curves (Fig. 22(f)) also display consistent trends among theoretical, numerical, and experimental approaches.

5.2. Dynamic experiments

This section focuses on the vibration isolation performance of the prototype through analyzing dynamic testing results. Experimental setup, illustrated in Fig. 23, includes a B&K PULSE system, accelerometers, a signal generator, an electrodynamic shaker, and a charge amplifier. Base excitation is provided by the shaker, with a 3D-printed rigid plate serving as the mounting platform. A rectangular slot machined into the plate houses the isolator, which is securely bonded using high-strength adhesive. Two accelerometers are installed: one to measure the base excitation, and the other the output response atop the isolator. A sinusoidal acceleration signal with an amplitude of 1 m/s^2 is applied, and the frequency is swept from 0 to 50 Hz. Each test is repeated three times to ensure reliability.

The isolation performance was experimentally evaluated in three directions with a payload mass of $M = 1.086$ kg. For Y-direction (vertical) isolation, a harmonic excitation of 1.45 mm amplitude was applied at the base plate center (Fig. 24 (a)). The measured acceleration response (Fig. 24 (b)) confirms effective isolation, and the transmissibility curves from experiments, ADAMS, and RK4 show good agreement (Fig. 24 (c)). Minor deviations are attributed to possible eccentricity or misalignment of the excitation mechanism. For X-direction (horizontal) isolation, a lateral excitation of 0.35 mm was applied using a guided rail with bilateral sliders (Fig. 24 (d)-(f)). The experimental transmissibility matches simulations well; discrepancies mainly arise from friction and rail misalignment. For θ-direction (rotational)

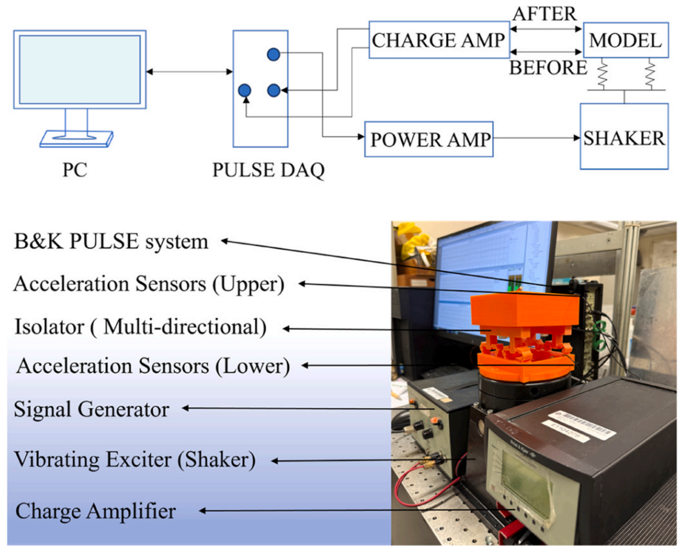

Fig. 23. Experimental equipment and setup.

isolation, an eccentric excitation of 0.298 rad was applied at the base (Fig. 24 (g)-(i)). Slight discrepancies between the experimental and simulated transmissibility curves are due to minor flutter during rotation, and load asymmetry. Overall, despite these minor deviations, the experiments confirm the theoretical and numerical findings regarding multi-direction isolation performance and the system's coupling characteristics.

6. Conclusions

This study presents a comprehensive theoretical and experimental analysis of a compact multi-directional vibration isolator. Notably, it addresses a key research gap by introducing a 3D-printed integrated design and a rigorously coupled dynamic model to elucidate the often-neglected directional coupling mechanisms. The main conclusions are:

1. Vertical (Y-direction) isolation exhibits strong robustness and can be effectively decoupled from the X and θ directions, due to their weak coupling effects.

2. Horizontal (X-direction) isolation deteriorates significantly under rotational coupling, with transmissibility increasing by up to 45% and the starting isolation frequency shifting upward. Phase diagrams further reveal notable velocity amplification and resonance intensification under multi-directional excitations.

3. Rotational (θ-direction) isolation displays amplitude-dependent nonlinearity, including an equilibrium offset. Its performance is impaired by coupling with the X-direction.

4. Directional coupling asymmetry governs energy transfer in the system. Rotational coupling should be considered in the design of X-direction isolators to avoid performance overestimation, while neglecting X-direction inputs may compromise θ-direction isolation.

These findings highlight the critical role of rotational-translational coupling in multi-directional isolation performance and provide invaluable insights for aerospace, and automotive engineering applications. Nevertheless, certain limitations of this investigation should be noted. The proposed model relies on simplifying assumptions, such as idealized rigid bodies and massless components, whose effects warrant further investigation under real operating conditions. The present study is limited to a single optimized configuration. A broader parametric exploration would better clarify performance trade-offs across all degrees of freedom. Equally necessary is a full nonlinear characterization, including stability evaluation, and bifurcation analysis. Looking forward, future investigations could also target systematic multi-objective optimization and establish a validated hybrid theoretical-experimental-

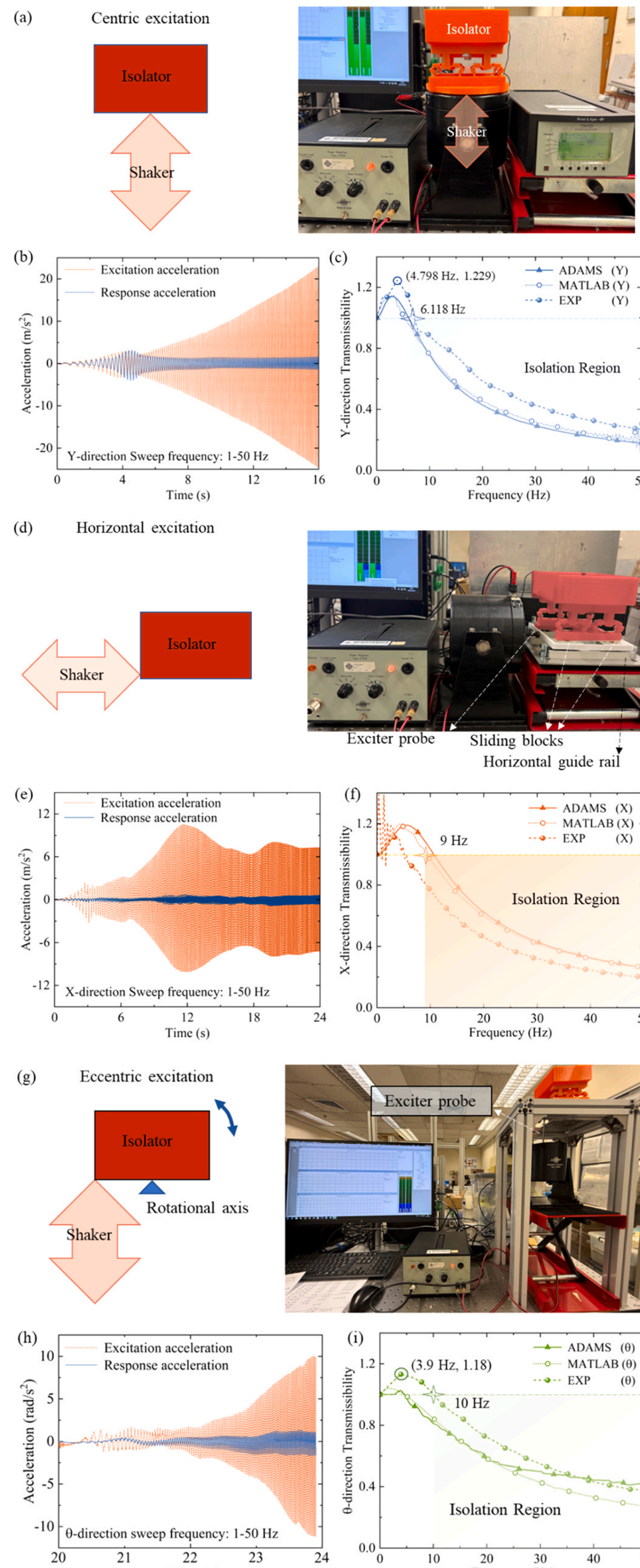

Fig. 24. Three-direction vibration experimental frame diagram, time-domain and frequency response: (a)-(c) Y-direction; (d)-(f) X-direction; (g)-(i) θ-direction.

numerical platform to support rapid prototyping and accurate prediction under realistic, multi-directional loading scenarios.

CRediT authorship contribution statement

Li Cheng: Writing – review & editing, Validation, Supervision, Resources, Project administration, Methodology, Funding acquisition, Conceptualization. **Xiuhui Hou:** Writing – review & editing, Supervision, Resources, Project administration, Funding acquisition. **Zichen Deng:** Writing – review & editing, Supervision, Resources, Project administration, Methodology, Funding acquisition. **Ge Yan:** Writing – review & editing, Validation, Methodology, Formal analysis, Conceptualization. **Xiang Yu:** Writing – review & editing, Visualization, Resources, Project administration, Funding acquisition, Conceptualization. **Mingzhu Jin:** Writing – review & editing, Writing – original draft, Validation, Software, Methodology, Investigation, Formal analysis, Conceptualization.

Declaration of Competing Interest

The authors declare that they have no known competing financial interests or personal relationships that could have appeared to influence the work reported in this paper.

Acknowledgements

The authors gratefully acknowledge the support by the National Natural Science Foundation of China (12572026, 12232015), National key R&D program of China (2024YFB3408700 and 2024YFB3408701), and the Doctoral Thesis Innovation Fund project of Northwestern Polytechnical University (06010–24GH01020101, CX2024003). The authors would like to thank Dr. NG Chun-hung, Stephen, Dr. Zhiyuan Li, and Dr. Jiajia Lu — Department of Mechanical Engineering, The Hong Kong Polytechnic University — for their help in the experiments, code check and review.

Data availability

Data will be made available on request.

References

[1] An XY, Yuan XF, Fan HL. Meta-Kagome lattice structures for broadband vibration isolation. Eng Struct 2023;277:115403.
[2] Ma HY, Xu PD, Fan WH, Yan B. Bionic Issus-inspired gear-driven structure with adjustable stiffness and rotational inertia properties for low-frequency vibration isolation. Mech Syst Signal Pr 2025;239:113331.
[3] Yu N, Tian FH, Ma HY, Cai CQ, Tang Y, Yan B. Tunable quasi-zero stiffness vibration isolators with electromagnetic damping for low-frequency vibration isolation enhancement. Mech Syst Signal Pr 2025;237:113082.
[4] Wu MK, Wu JL, Ren B, Gao RQ, Zhang FX, Zhou R, Bai YM, Li XQ, Chen XD, Jiang W. A linear planar magnetic spring for 2-DOF vibration isolation. Int J Mech Sci 2025;299:110432.
[5] Qi WH, Zhao TY, Gao QH, Lu JJ, Cai LQ, Li Y, Yan G, Zhang WM. 3-DOF decoupled magnetic platform for optical low-frequency vibration isolation. Int J Mech Sci 2025;300.
[6] Wang SH, Wang ZY, Wang B, Liu Z, Ni YZ, Lai WX, Jiang S, Huang YA. Experimental study of solid-liquid origami composite structures with improved impact resistance. Theo Appl Mech Lett 2024;14:100508.
[7] Ledezma-Ramírez DF, Tapia-Gonzalez PE, Ferguson N, Brennan M, Tang B. Recent advances in shock vibration isolation: an overview and future possibilities. Appl Mech Rev 2019;71.
[8] Kamesh D, Pandiyan R, Ghosal A. Passive vibration isolation of reaction wheel disturbances using a low frequency flexible space platform. J Sound Vib 2012;331:1310–30.
[9] Liu T, Li AQ. An innovative three-dimensional QZS vibration isolator and multi-stage vibration isolation platform design. Mech Syst Signal Pr 2025;237:113070.
[10] Wang YM, Sun YX, Chen XH, He S, Zhang JF, Hu JB, Bai L, Wang CH. Bionic Spiderweb lattice metamaterials for energy absorption and vibration isolation. Int J Mech Sci 2025;300:110386.
[11] Li XF, Zhao PY, Jing XJ. X-Stewart mechanism for vibration isolation with nonlinear translational-to-rotational motion properties. Int J Mech Sci 2025;303:110596.
[12] Liu CR, Wang JF, Zhang W, Yang XD, Guo XY, Liu T, Su XY. Synchronization of broadband energy harvesting and vibration mitigation via 1:2 internal resonance. Int J Mech Sci 2025;301:110503.
[13] Jiang GQ, Zang HX, Xiong YH, Shen YJ, Guo ZK, Yang Y, Li M. Design and vibration reduction performance analysis of a 6-DOF nonlinear vibration isolation platform by employing bio-inspired multi-joint X-structure. Nonlinear Dyn 2025;113:21119–50.
[14] Xu J, Sun XT. A multi-directional vibration isolator based on Quasi-Zero-Stiffness structure and time-delayed active control. Int J Mech Sci 2015;100:126–35.
[15] Hu XY, Zhou CY. A stable horizontal 3-DOF vibration isolation system with adjustable stiffness: Theoretical analysis and experiment. Mech Syst Signal Pr 2025;230:112631.
[16] Zhou CY, Song YZ, Sun H, Hu XY, Yang LP, Pu HY, Liu C. Design and experiment of an integrate 3-DOF adjustable QZS vibration isolation system with high-order stability. Mech Syst Signal Pr 2025;228:112483.
[17] Liu CR, Wang YW, Zhang W, Yu KP, Mao JJ, Shen H. Nonlinear dynamics of a magnetic vibration isolator with higher-order stable quasi-zero-stiffness. Mech Syst Signal Pr 2024;218:111584.
[18] Ou HF, Zeng J, Lin MQ, Wang YF, Zeng YJ, Fang X, Hu LL. Stair-Stepping metamaterial and the derived isolator for all-DOF vibrations with multi-payloads. Eng Struct 2025;330:119890.
[19] Yan G, Zou H-X, Wang S, Zhao L-C, Wu Z-Y, Zhang W-M. Bio-inspired toe-like structure for low-frequency vibration isolation. Mech Syst Signal Process 2022;162:108010.
[20] Yan G, Qi WH, Lu JJ, Liu FR, Yan H, Zhao LC, Wu ZY, Zhang WM. Bio-inspired multi-joint-collaborative vibration isolation. J Sound Vib 2024;568:118089.
[21] Wang YM, Chen XH, Sun YX, Zhang JF, Hu JB, Bai L. Full-band vibration isolation and energy absorption via cuttlebone-inspired lattice structures. Int J Mech Sci 2024;274:109283.
[22] Liu CR, Zhang W, Yu KP, Liu T, Zheng Y. Quasi-zero-stiffness vibration isolation: designs, improvements and applications. Eng Struct 2024;301:117282.
[23] Yang JH, Yang XD. Theoretical and experimental study of a novel nonlinear quasi-zero Stiffness vibration isolator based on a symmetric link-rod-type structure. Eng Struct 2024;301:117284.
[24] Song HN, Shan XB, Hou WJ, Wang C, Sun KW, Xie T. A novel piezoelectric-based active-passive vibration isolator for low-frequency vibration system and experimental analysis of vibration isolation performance. Energy 2023;278:127870.
[25] Zhang L, Zhang RF, Xie LY, Xue ST. Dynamics and isolation performance of a vibration isolator with a yoke-type nonlinear inerter. Int J Mech Sci 2023;254:108447.
[26] Ding BX, Li X, Chen SC, Li YM. Modular quasi-zero-stiffness isolator based on compliant constant-force mechanisms for low-frequency vibration isolation. J Vib Control 2024;30:3006–20.
[27] Cai JZ, Gao QB, Zhang XJ. Proportional-retarded control of a quasi-zero-stiffness vibration isolator. J Sound Vib 2024;578:118309.
[28] Li TY, Yu CL, Yu XY, Li B, Zhao B, Tian JB. Ultra-low frequency active vibration isolation system with quasi-zero stiffness characteristic using self-tuning filter-based feedforward control. J Sound Vib 2025;597:118848.
[29] Liu J, Wang M, Pu HY, Zhou SX, Li ZJ, Sun Y, Ding JH, Peng Y, Xie SR, Luo J. Theoretical and experimental analysis of symmetric and asymmetric magnet-based bistable vibration isolators. Mech Syst Signal Pr 2025;224:111956.
[30] Yu N, Fei XY, Sun H, Wu ZM, Yan B. Rhombus-type magnetic-levitation structure for low-frequency vibration isolation. Mech Syst Signal Pr 2025;225:112289.
[31] Chu TH, Tsai SH, Liang Y-J. Experimental and numerical study on vibration attenuation performance of 3D printed single-phase metamaterial plate with broad low-frequency complete bandgap. Eng Struct 2025;341:120875.
[32] Sui GD, Zhou CY, Chen YF, Zhang XF, Hou CW, Shan XB, Cao J. Research on flexible beam-type nonlinear vibration isolators suitable for low frequencies. Ocean Eng 2024;293:116652.
[33] Hou S, Wei JZ. A quasi-zero stiffness mechanism with monolithic flexible beams for low-frequency vibration isolation. Mech Syst Signal Pr 2024;210:111154.
[34] Lu JJ, Qi WH, Liu FR, Cao YB, Zhao TY, Cai LQ, Li Y, Yan G, Zhang WM. Compliant curved beam support with flexible stiffness modulation for near-zero frequency vibration isolation. J Sound Vib 2025;595:118702.
[35] Chen N, Zuo A, Jiang PF, Xu YL, Yang ZC. A ring metastructure vibration isolator with thin beams. Int J Mech Sci 2024;280:109528.
[36] Ba H, Niu MQ, Chen LQ. An adjustable stiffness vibration isolator implemented by a semicircular ring. Mech Syst Signal Pr 2025;222:111797.
[37] Xiao L, Sun X, Cheng L, Yu X. A 3D-printed quasi-zero-stiffness isolator for low-frequency vibration isolation: Modelling and experiments. J Sound Vib 2024;577:118308.
[38] Lu JJ, Yan G, Qi WH, Yan H, Liu FR, Zhao TY, Zhang WM. Integrated vibration isolation and actuation via dual nonlinear stiffness regulation. Int J Mech Sci 2024;263:108760.
[39] Hussain S, Hou XH, Zhang K, Deng ZC. Performance assessment of newly developed Quasi-Zero Stiffness Damper (QZSD) for seismic protection of steel frame structures. Int J Appl Mech 2025;17:2530001.
[40] Yan G, Lu JJ, Qi WH, Liu FR, Yan H, Zhao LC, Wu ZY, Zhang WM. Linear and nonlinear stiffness compensation for low-frequency vibration isolation: a comparative study. Nonlinear Dyn 2024;112:5955–73.
[41] Sun K, Tang J, Wu ZJ, Li YH, Cao DQ. Coupled nonlinear vibration characteristics of quasi-zero-stiffness Gough-Stewart isolation platform. Aerosp Sci Technol 2024;152:109352.

[42] Vu MH, Ngoc PVB, Thien NL. Kinematics design and statics analysis of novel 6-DOF passive vibration isolator with S-shaped legs based on Stewart platform. Adv Sci Technol Eng Syst J 2023;8:81–90.
[43] Tang J, Yang Y, Dou CH, Li YH, Cao DQ. Micro-vibration control of spaceborne payload with smart parallel struts. Mech Adv Mater Struct 2024;23:1–15.
[44] Wang S, Hu Y, Zhang T, Guo WY, Yu LD. Isolation performance of velocity-displacement-dependent damping on a general six-bar linkage system via the discrete incremental harmonic balance method. Nonlinear Dyn 2024;113:377–96.
[45] Li LZ, Meng WN, Bao Y. Bandgap metamaterials for vibration control: Theories, design, fabrication, and applications. Eng Struct 2026;347:121746.
[46] Croce P, Orsini P, Salvatore W. Vibration isolation and design of automotive test benches. Eng Struct 2001;23:945–56.
[47] Li Y, Chang YP, Zhou JX, Wang K. Dual quasi-zero-stiffness dynamic vibration absorbers for double-low-frequency vibration suppression. Int J Mech Sci 2024;264:108852.
[48] Li H, Bi KM, Han Q, Ma RS. A state-of-the-art review on negative stiffness-based structural vibration control. Eng Struct 2025;323:119247.
[49] Liu WL, Wu LL, Sun JB, Zhou J. Origami-inspired quasi-zero stiffness metamaterials for low-frequency multi-direction vibration isolation. Appl Phys Lett 2023;123:084102.
[50] Shao ZP, Bai W, Dai JW, Yu H, Wu BY, Liang JK. Research on the effectiveness of a new-type bearing for structural seismic and vibration dual control. Struc 2024;62:106188.
[51] Han QK, Gao S, Chu FL. Micro-Vibration Analysis, Suppression, and Isolation of Spacecraft Flywheel Rotor Systems. A Rev 2024;Vib. 7:229–63.
[52] Hao RB, Lu ZQ, Ding H, Chen LQ. Shock isolation of an orthogonal six-DOFs platform with high-static-low-dynamic stiffness. J Appl Mech 2023;90:1–30.
[53] Huang XB, Wang B, Huang ZW, Hua XG, Chen ZQ. A theoretical model for a low-frequency two-stage hybrid vibration isolator with a nonlinear energy sink and a negative stiffness spring. Appl Math Model 2025;142:115948.
[54] Rui ST, Yang SK, Zheng PY, Wang XZ, Han B, Ma FY. Self-contacting overlay complementary multi-level multi-stable quasi-zero stiffness vibration isolation device. Mech Syst Signal Pr 2025;226:112340.
[55] Wu MK, Gao RQ, Zhou YF, Che JX, Wu JL, Li XQ, Chen XD, Jiang W. Analysis and experiment of a multi-tile magnetic spring with high negative stiffness. Mech Syst Signal Pr 2025;223:111914.
[56] Chen P, Deng YY, Zhou DS, Ma KQ. A novel disc spring set for vertical vibration isolation: Experimental test, modeling and comparative analysis. Eng Struct 2025;339:120554.
[57] Lin QD, Zhou JX, Quqa S, Palermo A, Marzani A, Wang K, Wang Q, Pu XB. Harnessing quasiperiodic pattern to widen the low-frequency band gap of quasi-zero-stiffness metamaterials. Thin Walled Struct 2025;214:113393.
[58] Li LB, Yang F, Liu SF, Guo ZM, Han D, Xia Y, Wang LH, Fan HL. Design of quasi-zero-stiffness metamaterials with ultra-wideband vibration isolation performance. Int J Mech Sci 2025;300:110440.
[59] Chen YH, Niu MQ, Fan YM, Chen LQ. Quasi-zero-stiffness vibration isolation via a double-layer compliant mechanism. Int J Mech Sci 2025:110670.
[60] Lu JB, Cai QL, Zhu SY. Superior vibration isolation performance of inerter dampers for SDOF structures under narrowband random excitations. Eng Struct 2025;326:119413.
[61] Zhang RR, Yang YF, Ma C, Jiang J, Liu X, Yue HH, Lu YF. A novel low-stiffness blade gear for micro-vibration isolation: Design, modeling, and verification. Mech Syst Signal Pr 2024;211:111223.
[62] Liang QH, Luo WL, Zhou Y, Lu ZC, Li JR, He ZM. Vibration filtering effect of a novel three-dimensional isolation bearing on metro vibration isolation. Eng Struct 2024;301:117304.
[63] Lu ZQ, Hao RB, Wu D, Ding H, Chen LQ. An investigation of a self-powered low-frequency nonlinear vibration isolation system. Eng Struct 2024;315:118395.
[64] Ye K, Ji JC. Dynamic analysis of the effects of self-weight induced structural and damping nonlinearity on the performance of an origami-inspired vibration isolator. J Sound Vib 2023;547:117538.
[65] Sun K, Tang J, Wu ZJ, Li YH, Cao DQ. Coupled nonlinear vibration characteristics of quasi-zero-stiffness Gough-Stewart isolation platform. Aerosp Sci Technol 2024;152:109352.
[66] Zhang XW, Wang XP, Ye YR. Asymmetric design enables self-coupled locally resonant metastructure for multi-modal vibration isolation. Mech Syst Signal Process 2026;248:113984.
[67] Xing Z, Tang J, Min Q, Li M, Li YH, Chen HT, Cao DQ. Model predictive vibration control for a six-degree-of-freedom rigid-flexible coupled parallel platform. Thin Walled Struct 2026;228:115061.
[68] Zhan QC, Zhao YH, Ouakad H. A theoretical and experimental study on the vibration control of a coupled beam system using a series-coupled dual oscillator system model. Mech Syst Signal Process 2026;242:113608.
[69] Fang P, He ZH, Wang XQ, Hou YJ. Dynamic synchronization and stability for dual-motor anti-resonance system coupled with a tension spring. Trans Can Soc Mech Eng 2026;50:1–16.
[70] Wang QS, Wang RH, Zhong R, Wu X, Duan JA. Nonlinear dynamic of aircraft-like shell coupled with internal nonlinear components. Mech Syst Signal Process 2026;249:114049.
[71] de Castro CHL, Orlando D, Gonçalves PB. Static and dynamic nonlinear behavior and instabilities of a multistable system consisting of two shallow coupled arches. Int J Non-Linear Mech 2025;174:105087.
[72] Alanazy A, Moatimid GM, Amer TS, Mohamed MAA. An innovative methodology in analyzing two-degrees-of-freedom of coupled dynamical system. Ain Shams Eng J 2025;16:103770.
[73] Liu JF, Lou JJ, Chai K, Yang QC. Nonlinear vibration-acoustic analysis of the coupled system of flexible cylindrical shell foundation and HSLDS vibration isolator. Thin Walled Struct 2025;209:112896.
[74] Ma HW, Ji WH, Zhang Y, Zhang H, Liu HH, Sun W. Frequency veering and coupled vibration of fluid-transporting parallel pipeline systems with constrained layer damping. Ocean Eng 2025;321:120306.
[75] Cui XL, Chen J, Huang B, Luo WL, Li K, Cheng L, Zhong D, Ai PP, Fan SX. Coupled dynamics and resonance mitigation of submerged floating tunnel roadways under transient impact loads in marine environments. Ocean Eng 2026;358:125830.
[76] Li ZZ, Zhong R, Wang RH, Wang QS, Qin B. Nonlinear dynamic analysis of the double-layer lattice sandwich circular plate and nonlinear vibration absorber coupled system. Compos Struct 2025;371:119475.
[77] Yang T, Cao QJ. Modeling and analysis of a novel multi-directional micro-vibration isolator with spring suspension struts. Arch Appl Mech 2022;92:801–19.
[78] Preumont A, Horodinca M, Romanescu I, de Marneffe B, Avraam M, Deraemaeker A, Bossens F, Abu Hanieh A. A six-axis single-stage active vibration isolator based on Stewart platform. J Sound Vib 2007;300:644–61.